Systematic recovery of instrumental timing and phase errors using interferometric surface-waves retrieved from large-N seismic arrays

Weemstra, Cornelis; De Laat, Janneke I.; Verdel, Arie; Smets, Pieter

DOI
10.1093/gji/ggaa504

Publication date
2020

Document Version
Final published version

Published in
Geophysical Journal International

Geophysical Journal International

Geophys. J. Int. (2021) **224,** 1028–1055
Advance Access publication 2020 October 20
GJI Seismology

doi: 10.1093/gji/ggaa504

Systematic recovery of instrumental timing and phase errors using interferometric surface-waves retrieved from large-N seismic arrays

Cornelis Weemstra [1,2] Janneke I. de Laat,[3] Arie Verdel[4] and Pieter Smets [1,2]

[1] *Department of Geoscience and Engineering, Delft University of Technology, Delft, The Netherlands. E-mail: kweemstra@gmail.com*
[2] *Royal Netherlands Meteorological Institute, De Bilt, The Netherlands*
[3] *Dublin Institute for Advanced Studies, Dublin, Ireland*
[4] *Netherlands Organization for Applied Scientific Research (TNO), Utrecht, The Netherlands*

Accepted 2020 October 15. Received 2020 October 14; in original form 2020 May 27

SUMMARY

Instrumental timing and phase errors are a notorious problem in seismic data acquisition and processing. These can be frequency independent, for example due to clock drift, but may also be frequency dependent, for example due to imperfectly known instrument responses. A technique is presented that allows both types of errors to be recovered in a systematic fashion. The methodology relies on the time-symmetry usually inherent in time-averaged cross-correlations of ambient seismic noise: the difference between the arrival time of the direct surface-wave at positive time and the arrival time of the direct surface-wave at negative time is quantified. Doing this for all eligible receiver–receiver pairs of a large-N seismic array, including one or more receivers devoid of instrumental timing errors, the instrumental timing errors of all incorrectly timed receivers can be determined uniquely. Most notably, this is accomplished by means of a weighted least-squares inversion. The weights are based on the receiver–receiver distances and decrease the adverse effect of inhomogeneities in the noise illumination pattern on the recovered instrumental timing errors. Inversion results are furthermore optimized by limiting the inversion to receiver couples that (i) exceed a specific receiver–receiver distance threshold and (ii) whose time-averaged cross-correlations exceed a specific signal-to-noise ratio threshold. Potential frequency dependence of the timing errors is incorporated by means of an iterative, frequency-dependent approach. The proposed methodology is validated using synthetic recordings of ambient seismic surface-wave noise due to an arbitrary non-uniform illumination pattern. The methodology is successfully applied to time-averaged cross-correlations of field recordings of ambient seismic noise on and around the Reykjanes peninsula, SW Iceland.

Key words: Inverse theory; Seismic instruments; Seismic interferometry; Seismic noise; Surface-waves and free oscillations.

1 INTRODUCTION

Timing and phase errors are a notorious problem in seismic data acquisition. Instrument responses of differential pressure gauges (DPGs), for example, are usually imperfectly known due to the their dependence on the viscosity of the fluid and the diameter (and hence potential deterioration) of the capillary tube (Cox *et al*. 1984). In order to utilize DPG recordings in seismological traveltime studies, one therefore first needs to recover the unknown phase errors, and correct the recordings accordingly (e.g. Takeo *et al*. 2014). In the exploration industry, seismic reservoir monitoring relies on long-term clock stability (e.g. Shimizu *et al*. 2019). In the absence of such stability, timing errors incurred over time may lead to erroneous conclusions regarding changes in the reservoir. Similarly, regional ocean bottom networks, often deployed for the purpose of tomographic imaging, may suffer from clock drift of constituent ocean bottom seismometers (OBSs) (e.g. Gouédard *et al*. 2014; Takeo *et al*. 2014; Hable *et al*. 2018; Le *et al*. 2018). In this case, the timing errors may result in erroneous seismic images and hence false geological interpretations.

The introduction of seismic interferometry (SI) in the seismological community has resulted in a number of studies devoted to the recovery of instrumental timing errors (e.g. Stehly *et al*. 2007; Sens-Schönfelder 2008; Hatchell & Mehta 2010; Hannemann *et al*. 2013). Seismic interferometry (SI) refers to the principle of generating new seismic responses from existing recordings (Wapenaar & Fokkema 2006). For the purpose of recovering timing errors, SI is generally applied to passive seismic wave fields (e.g. Ye *et al*. 2018). In that context, simple

time averaging of noise cross-correlations often suffices to generate a new seismic response (e.g. Shapiro & Campillo 2004; Weemstra *et al*. 2013). Essentially, the cross-correlation process turns one receiver into a so-called 'virtual source', whose response is retrieved at another receiver (e.g. Bakulin & Calvert 2006). In case the passive seismic wave field illuminates the receiver pair from all angles, two virtual-source responses will be retrieved: the response to one virtual source (associated with one of the two receivers) results in arrivals in the time-averaged cross-correlation at positive time, whereas the response to the other virtual source (associated with the other receiver) results in arrivals in the time-averaged cross-correlation at negative time (e.g. Stehly *et al*. 2006; Weemstra *et al*. 2013). Under specific conditions, these virtual-source responses can be related to the Green's function of the medium (Malcolm *et al*. 2004; Snieder 2004; Wapenaar & Fokkema 2006).

In this study, we will restrict ourselves to the surface-wave part of the Green's function and focus on surface-wave arrivals in the 0.1–0.5 Hz frequency range. In practice, also body-wave energy is observed in recordings of ambient seismic noise (e.g. Gerstoft *et al*. 2008; Poli *et al*. 2012). Between 0.1 and 0.5 Hz, however, the amplitude of the body waves is (generally) considerably lower than the amplitude of the surface-waves. This can be explained by the fact that surface-waves propagate in directions parallel to the surface of the Earth (cylindrical spreading), whereas body-wave energy spreads in three dimensions (spherical spreading, e.g. Aki & Richards 2002). The amplitude decay due to geometrical spreading is consequently much smaller for surface-waves than for body waves. The fact that most of the seismic noise in this frequency range is generated by interaction of ocean surface gravity waves (the so-called 'microseisms'; Longuet-Higgins 1950; Hasselmann 1963), that is, relatively far away in terms of wavelengths, intensifies the difference between surface- and body-wave energy.

When it comes to the interferometric recovery of timing errors, two approaches can be distinguished (Gouédard *et al*. 2014). The first approach relies on the (presumed) temporal stability of time-averaged cross-correlations. In this approach, virtual-source responses are retrieved in a time-lapse manner to recover temporal variations in timing errors (e.g. clock drift; Hable *et al*. 2018). Specifically, in application to ambient seismic surface-wave noise, time-lapse changes in the arrival times of the direct interferometric surface-waves are used for this purpose. This approach generally recovers timing errors using time-averaged cross-correlations computed between single pairs of stations. As such, one of the two stations needs to be devoid of timing errors, whereas the recordings by the other station can be subject to timing/clock errors. The latter station, however, is required to have zero timing error at a specific reference time. For this approach, it suffices if only a virtual-source response at positive time, or a virtual-source response at negative time is retrieved (in a time-lapse manner). The second approach exploits the (theoretical) pairwise time symmetry of the time-averaged cross-correlations to recover timing errors (e.g. Stehly *et al*. 2007; Sens-Schönfelder 2008; Hatchell & Mehta 2010). Contrary to the first approach, both a direct surface-wave arrival at positive time and a direct surface-wave arrival at negative time need to be retrieved in this case. Similar to the first approach, however, one of the two stations needs to be devoid of timing errors. Importantly, and contrary to the first approach, the recordings by the other station need not be subject to a zero timing error at a specific reference time. Since our data set contains stations whose recordings are subject to a fixed timing error (i.e. not zero at a specific reference time), we adopt and investigate the second approach in this study.

Both aforementioned approaches have in common that they suffer from deviations from a uniform surface-wave illumination. In the first approach, potential variations in surface-wave arrival times due to a time varying surface-wave illumination pattern (e.g. Weaver *et al*. 2009; Froment *et al*. 2010) may adversely affect the accuracy of the recovered timing errors. In the second approach, a non-uniform illumination pattern may break the time-symmetry. Consequently, the recovered timing errors deviate from the correct (unknown) timing errors. In this study, we show that a weighted (least-squares) inversion mitigates the effect of an anisotropic surface-wave illumination on the recovered timing errors and hence reduces the deviations of the recovered timing errors from the actual timing errors.

As mentioned at the beginning of this section, timing errors may arise from the lack of well-defined instrument responses (e.g. Takeo *et al*. 2014). In addition, however, timing errors could also be the result of applying an erroneous instrument correction. That is, a (theoretical) transfer function that does not correctly predict the actual modification of the phase of the recorded signal. This is partly the case in this study (as we will detail in Section 2). It is for this reason, that, in this study, we independently estimate timing errors for different frequency bands. Consequently, we allow frequency-dependent timing errors, which may be the result of (potentially frequency-independent) phase errors, to be recovered. The methodology presented in this study has been implemented in fortran, and the code has been made freely available (see Acknowledgements).

In this study, the pairwise time symmetry of the time-averaged cross-correlations is exploited. This is done using ambient seismic noise recorded by an array of seismic stations on and around the Reykjanes peninsula, SW Iceland. In the following section, we introduce the data characteristics and give a motivation for using this particular data set. In Section 3, subsequently, we briefly summarize the theory underlying SI by cross-correlation. In Section 4, we introduce the (forward) model for the instrumental timing errors. From this model, an ordinary least-squares inversion and two weighted least squares inversions are derived. Before we introduce these inversions, however, we detail in Section 5 how the measurements are obtained in an automated fashion. In particular for so-called large-N seismic arrays, this is essential. The ordinary and weighted least-squares inversions are introduced in Sections 6 and 7, respectively. All inversions are tested by means of synthetic recordings of ambient seismic noise. In Section 8, we focus on two important parameters that determine the quality of the measurements and hence of the inversions. These are the minimum signal-to-noise ratio (SNR) of the virtual source responses at positive and negative time, and the minimum distance two stations need to be separated in order to qualify as eligible measurement. Finally, in Section 9, we apply the inversions to time-averaged cross-correlations of ambient seismic noise recorded during 2014 and 2015, after which we end by listing our conclusions (Section 10).

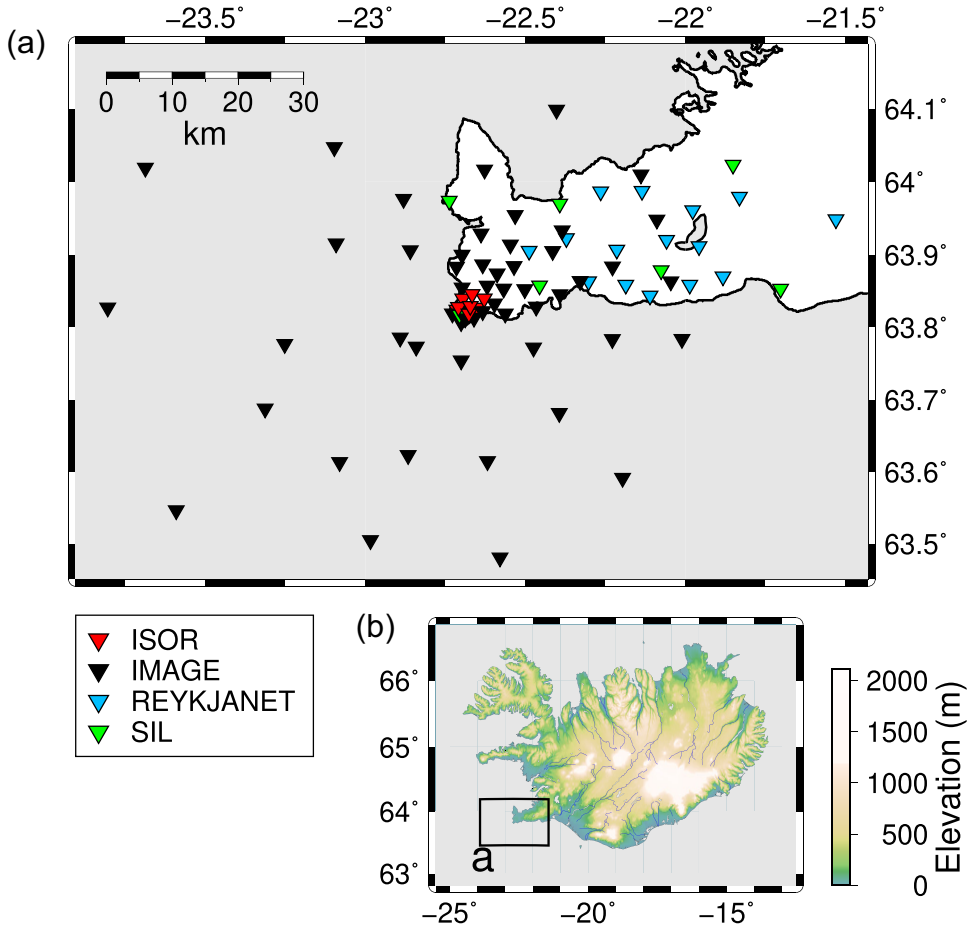

Figure 1. (a) The station configuration of the RARR and (b) its location.

2 DATA AND MOTIVATION

This study is motivated by our analysis of the ambient seismic noise recorded by what we refer to as the Reykjanes Array (RARR); a subset of this seismic array has recently been used for the purpose of ambient noise surface-wave tomography (Martins *et al*. 2020). The RARR was a dense seismic deployment on and around the Reykjanes peninsula, SW Iceland (Fig. 1). It was a composite array formed using stations from four different seismic networks/deployments and active from April 2014 until August 2015 (an overview of the data availability as function of time can be found in Fig. S1). The bulk of the stations (53) were deployed in the context of IMAGE (Integrated Methods for Advanced Geothermal Exploration, black). This number includes 23 ocean bottom seismometers (OBSs). Another 15 stations constitute REYKJANET (lightblue), which was operated by the Iceland GeoSurvey (ISOR) on behalf of the institute of geophysics of the Czech Academy of Sciences (CAS). The deployment referred to as 'ISOR' (red) consisted of 8 stations and was also operated by ISOR, but on behalf of HS Orka, the operator of a geothermal power plant on the tip of Reykjanes. Finally, 7 stations were part of the SIL network (green) and were operated by the Icelandic meteorological office (MET office). All 83 stations are equipped with 3-component sensors, but we restricted this study to recordings by the vertical components.

The IMAGE seismic campaign has been initiated to assess the potential of SI in the context of geothermal exploration. Since ambient noise surface-wave tomography is an established application of SI, we would like to exploit the noise recordings by all stations of the RARR for this purpose. In particular, we aim to solve the tomographic inverse problem using interferometric responses between 0.1 and 0.5 Hz. Generally speaking, the higher the number of available ray paths crossing the medium under investigation, the better (seismic) tomography is able to constrain this medium. It is therefore desirable to exploit noise recordings by as many stations as possible. An overview of the types of sensors that make up the RARR is given in Table 1. We show in Section 3 that despite the relatively high corner frequency of some of these instruments (transfer functions are provided as Figs S2 and S3), most receiver–receiver cross-correlations result in sufficiently energetic surface-wave responses for the extraction of receiver–receiver phase velocities.

Evidently, the extraction of receiver–receiver phase (or group) velocities from interferometric responses requires accurate timing of the noise recordings. At frequencies between 0.1 and 0.5 Hz, however, the recordings by many of the RARR stations remain subject to time shifts after removal of the instrument responses (despite the aforementioned high amplitude of the retrieved surface-wave responses). The OBS recordings, for example, are subject to clock errors arising from the lack of a GPS connection below the sea surface (e.g. Shariat-Panahi *et al*. 2009). Also, communication with the institute of geophysics of the CAS (Josef Horalek 2016, personal communication) taught us that

Table 1. Instruments and stations comprising the RARR. Note that the OBSs are numbered up to 26, but that 3 are missing (O09, O13, O24), because, for various reasons, these did not provide any data (see Fig. S1). The last column indicates, for frequencies lower than 1 Hz, which groups of stations have demonstrated to be subject to timing errors (REYKJANET, ISOR and SIL stations) or are suspected to be subject to timing errors (the OBSs of IMAGE), and which not (the stations equipped with the *Trillium compact 120s* and *Mark L-4C-3D* sensors).

Network/deployment	Instrument	Stations	Timing (<1 Hz)
IMAGE	*Trillium compact 120s*	BER, GEV, EIN, HAH, HAS,	✓
(53 stations)	(20 stations)	HOS, KEF, KUG, LFE, ONG, PAT, PRE, RAH, RAR, RET, SDV, SKG, SKH, STA, SUH	
	Mark L-4C-3D sensor	NEW, HOP, KHR, KRV, SKF,	✓
	(10 stations)	STF, STK, VSV, ARN, MER	
	Güralp-40T (OBSs)	O01, O02, O03, O04, O05,	✗
	(23 stations)	O06, O07, O08, O10, O11, O12, O14, O15, O16, O17, O18, O19, O20, O21, O22, O23, O25, O26	
REYKJANET	*Güralp-40T*	FAF, HRG, KLV, LSF, ELB,	✗
(15 stations)	(9 stations)	LAT, LHL, STH, MOH	
	Lennartz 3D/1s	ASH, SEA, ISS, GEI, LAG,	✗
	(6 stations)	HDV	
ISOR	*Lennartz 3D/1s*	UNN, ANG, TMN, TMS, YRA,	✗
(8 stations)	(8 stations)	YRD, YRN, DBG	
SIL	*Lennartz 3D/5s*	GRV, NYL, RNE, VOG, KRI,	✗
(7 stations)	(7 stations)	VOS, KAS	

the *Lennartz 3D/1s* is a simple commercial 4.5 Hz geophone, which is over-damped by a negative damping resistance (special circuit, not feedback). This implies that the instrument response is electronically extended down to 1.0 Hz, such that the instrument response is well defined between 1.0 and 80.0 Hz. Due to the negative resistance, however, the instrument response is not guaranteed below 1 Hz; particularly the phase response may differ significantly from the theoretical one, resulting in time shifts remaining after removal of the instrument response. Despite the erroneous phase response below 1.0 Hz, the sensors are sensitive enough to recover vertical particle velocity between 0.1 and 0.5 Hz and hence allow the retrieval of interferometric surface-wave responses. For some of the instruments (e.g. the *Güralp-40T* instruments of REYKJANET), however, we cannot explain the observed time shifts. Perhaps the theoretical phase responses of these instruments is also not accurate below a certain frequency. The stations equipped with the *Trillium compact* and *Mark L-4C-3D* instruments, which together constitute the IMAGE stations deployed on land (30 in total), did not exhibit a time-shift after removal of the instrument response. The latter we concluded based on the fact that the recordings by these two types of instruments appeared to be consistent with each other after removal of the instrument response. Also, the theoretical phase response is close to zero between 0.1 and 0.5 Hz for these instruments, as these are broadband sensors (see the transfer functions in Figs S2 and S3). We have indicated in Table 1 whether a station's timing is prone to errors (✗), or not (✓). In the remainder of the text, the superscripts $^{\checkmark}$ and $^{\times}$ indicate whether a station's timing is correct or not, respectively. To lighten notational burden, we did not indicate this in the figures (but it should be clear from the captions).

In Fig. 2, we demonstrate how the surface-waves generated by a distant earthquake bear witness of the incurred time shifts. For this purpose, we focus on the tip of the Reykjanes peninsula, where the station density is highest: the tip of the peninsula is approximately 5 km by 5 km and host to all eight ISOR stations, as well as nine IMAGE stations. The fact that the surface-waves recorded by the eight ISOR stations do not align with the surface-waves recorded by the nine IMAGE stations strongly suggest the presence of timing errors (Fig. 2c). Frequency–wavenumber analysis (Lacoss *et al*. 1969; Rost & Thomas 2002), which is often referred to as 'beamforming', supports this: the resulting most likely slowness vector at 0.16 Hz (i.e. the so-called best beam), which is computed using only the recordings by the nine IMAGE stations, does not predict the phases of the recordings by the ISOR stations correctly (Fig. 2f). Taking into account that the surface-waves in Fig. 2 have an approximate wavelength of 25 km, it is highly unlikely that the time shifts observed in Fig. 2 are the result of local medium heterogeneities. That is, the observed time shifts are most probably due to the fact that the theoretical transfer function of the ISOR stations does not correctly predict the actual modification of the recordings (at these frequencies). The supporting material contains a two additional examples using different sets of closely separated stations and/or different earthquakes (Figs S4 and S5). At this point, it is

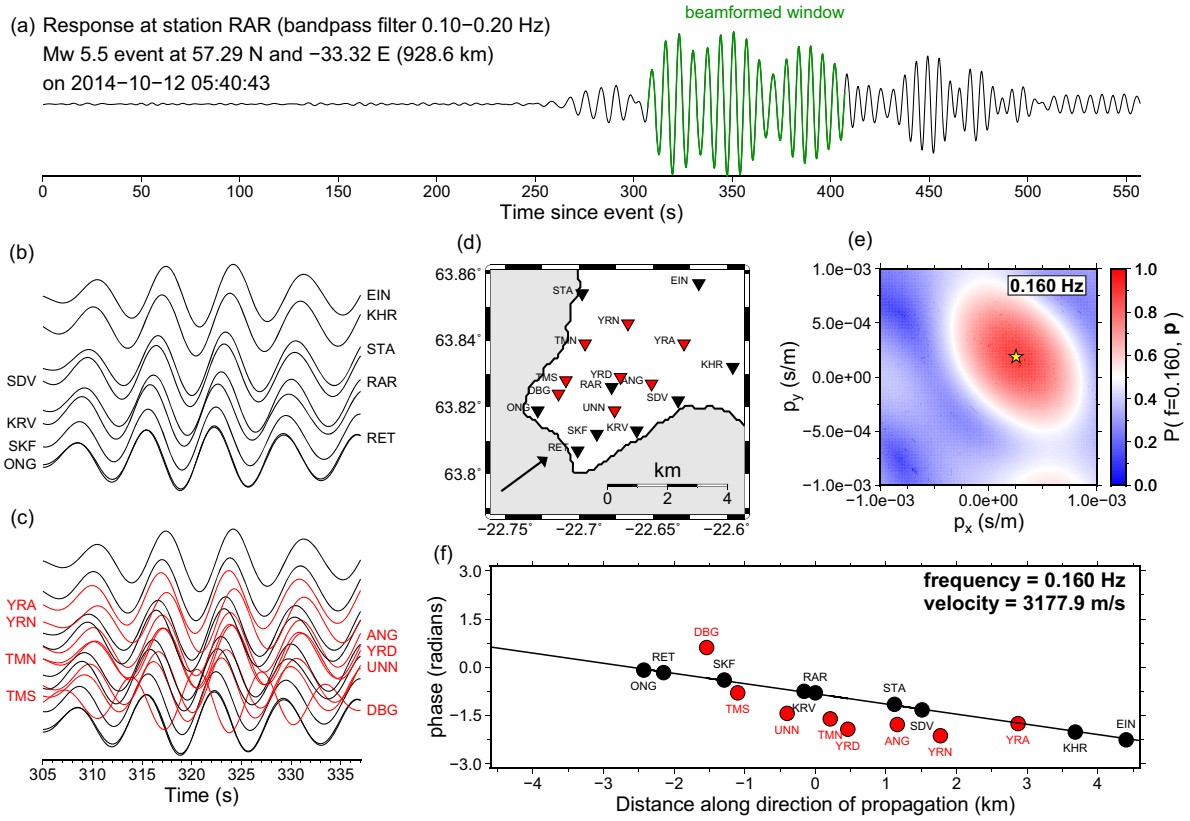

Figure 2. Analysis of the surface-waves generated by a Mw 5.5 earthquake along the Mid-Atlantic Ridge at a distance of approximately 930 km from the tip of the Reykjanes peninsula. (a) The surface-waves, bandpass filtered between 0.1 and 0.2 Hz, recorded by station RAR✓ (note that body wave energy is negligible in this frequency band). (b) Zoom of the earthquake's surface-waves recorded by nine IMAGE stations on the tip of the peninsula. A trace's position along the vertical axis increases proportional to its increase in distance from the earthquake's epicentre. (c) Same as b, but including the eight ISOR stations. (d) Location of the stations located on the tip of the peninsula. The arrow indicates the approximate direction of propagation of the surface-wave train indicated in green in a, as determined by frequency–wavenumber analysis at 0.16 Hz using only the nine IMAGE stations. (e) Result of frequency–wavenumber analysis at 0.16 Hz using only the nine IMAGE stations. Beamformer output is given as function of horizontal and vertical slowness (p_x and p_y, respectively). (f) Unwrapped phase at 0.16 Hz. Phases are obtained through Fourier transformation of the surface-waves arriving in the time window for which frequency–wavenumber analysis was performed. The slope of the solid black line corresponds to the slowness indicated by the yellow star in (e) (i.e. the so-called 'best beam'). This line is subsequently fitted, in least-squares sense, to the unwrapped phases of the nine IMAGE stations.

useful to note that we do not explicitly attempt to recover a frequency-dependent phase error in this study, but merely a frequency-dependent timing error (note that a clock error results in a linear, frequency-dependent phase error and, similarly, a frequency-independent phase error in a linear, frequency-dependent timing error). Notwithstanding, by independently estimating timing errors for different frequency bands, we effectively obtain frequency-dependent phase errors in Section 9.

3 SEISMIC INTERFEROMETRY BY CROSS-CORRELATION

Consider two seismic stations: a first station, S_i, located at $\mathbf{x}_i$ and a second station S_j, located at $\mathbf{x}_j$. We denote the azimuth of the vector pointing from $\mathbf{x}_i$ to $\mathbf{x}_j$ by $\theta_{i,j}$ (measured counterclockwise from North) and the vertical particle velocity at $\mathbf{x}_i$ and $\mathbf{x}_j$ by v_i and v_j, respectively. The time-domain cross-correlation $C^T_{i,j}$ is then defined as,

$$C^T_{i,j}(t) \equiv \frac{1}{2T}\int_{-T}^{T} v_i(\tau)v_j(\tau+t)\mathrm{d}\tau, \tag{1}$$

where t is time, τ is integration time and where we have normalized with respect to the length of the used (noise) cross-correlation window, that is T. We assume the length of this cross-correlation window to be sufficiently long with respect to the longest period within the frequency range of interest, that is $T \gg 1/\omega$, with ω the angular frequency. The explicit superscript T in $C^T_{i,j}$ indicates that $C^T_{i,j}$ is associated with a single time window (e.g. Tsai 2010; Weemstra *et al.* 2014), as opposed to the ensemble-averaged (or time averaged-averaged) cross-correlation introduced further below. Note that signal that is recorded at $\mathbf{x}_i$ prior to the time of recording at $\mathbf{x}_j$ will peak at positive time, whereas signal passing $\mathbf{x}_j$ before $\mathbf{x}_i$ will peak at negative time. We define the frequency domain cross-correlation, that is, the cross-spectrum, as $\hat{C}^T_{i,j}(\omega) \equiv \mathbf{F}[C^T_{i,j}(t)]$, where $\mathbf{F}$ is the temporal Fourier-transform.

In case several (noise) sources are acting simultaneously within a period of length T, spurious traveltime delays arise due to constructive interference of signal coming from different sources (e.g. Weemstra *et al*. 2014). Cancellation of these spurious arrivals is a requirement for the successful retrieval of interferometric receiver–receiver signal and can be achieved through ensemble averaging (e.g. Wapenaar & Fokkema 2006; Hanasoge 2013). In practice, ensemble averaging is replaced by integrating over sufficiently long time and/or averaging over several cross-correlation windows (e.g. Weemstra *et al*. 2017). We define the ensemble-averaged cross-correlation as $C_{i,j}(t) \equiv \left\langle C^T_{i,j}(t) \right\rangle$. The ensemble-averaged cross-correlation $C_{i,j}(t)$ can be related to the Green's function between $\mathbf{x}_i$ and $\mathbf{x}_j$ if a number of conditions are fulfilled: (i) the noise sources illuminate the station couple uniformly from all angles, (ii) the sources have coinciding amplitude spectra and (iii) the medium is lossless. Under these assumptions the ensemble-averaged cross-correlation will be proportional to the Green's function $G\left(\mathbf{x}_j, \mathbf{x}_i, t\right)$ and its time-reversed version, convolved with the autocorrelation of the signal emitted by the (noise) sources (Wapenaar & Fokkema 2006), that is,

$$C_{i,j}(t) \propto \left[G\left(\mathbf{x}_j, \mathbf{x}_i, t\right) + G\left(\mathbf{x}_j, \mathbf{x}_i, -t\right)\right] * P(t), \tag{2}$$

where the in-line asterisk $*$ denotes temporal convolution and where $P(t)$ denotes the autocorrelation of the signal of the (noise) sources.

In this study, we will restrict ourselves to the surface-wave part of the Green's function. Exploiting ambient seismic noise to accurately retrieve the surface-wave part of the Green's function requires an additional condition to be fulfilled. That is, the ambient noise wave field should be dominated by a single surface-wave mode (Halliday & Curtis 2008). Under the assumption that also this criterion is fulfilled, the ensemble-averaged noise cross-correlation has been shown to coincide with the surface-wave part of the Green's function plus its time-reversed version. We note that in the presence of heterogeneity, this Green's function will contain both direct and scattered arrivals and hence so will $C_{i,j}(t)$ (Boschi & Weemstra 2015). In this work we will focus on the direct surface-wave arrivals. Henceforth, we will simply use the term 'direct wave' (or 'direct response') to refer to the direct part of the surface-wave response.

In practice, eq. (2) is often not exact, that is, the Green's function (and its time-reversed version) are not accurately retrieved. This may be due to a number of reasons. The most notable probably being the fact that the illumination pattern is often non-uniform (Stehly *et al*. 2006; Mulargia 2012). A non-uniform illumination pattern leads to deviations of the retrieved surface-wave responses from the actual, correct surface-wave responses (Tsai 2009; Weaver *et al*. 2009). This, in turn, may result in inaccurate phase and/or group velocity measurements. Nevertheless, in case ambient surface-wave energy is propagating in both directions along the line connecting $\mathbf{x}_i$ and $\mathbf{x}_j$, a direct surface-wave response will be retrieved at both negative and positive time. Consider, for example, the stations KEF$^{\checkmark}$ and RAR$^{\checkmark}$, both equipped with broadband sensors. Fig. 3 presents the result of the application of SI to the vertical-component noise recordings by these two stations (black lines/symbols). Between 0.2 and 0.8 Hz, the propagation of surface-wave energy in both directions is manifested by the fact that at both positive and negative time a clear arrival can be discerned, representing estimates of $G\left(\mathbf{x}_j, \mathbf{x}_i, t\right)$ and $G\left(\mathbf{x}_j, \mathbf{x}_i, -t\right)$, respectively (we refer to Section 9 for a description of the data processing).

Fig. 3 also exemplifies the effect of the observed instrumental time shifts when it comes to tomographic surface-wave imaging. In addition to station couple KEF$^{\checkmark}$–RAR$^{\checkmark}$, we therefore evaluated the time-averaged cross-correlation of the station couple KEF$^{\checkmark}$–YRD$^{\times}$. Whereas stations KEF$^{\checkmark}$ and RAR$^{\checkmark}$ are equipped with broadband sensors, ISOR station YRD$^{\times}$ is equipped with a *Lennartz 3D/1s* geophone. The ray path connecting KEF$^{\checkmark}$ and RAR$^{\checkmark}$ nearly coincides with the ray path connecting KEF$^{\checkmark}$ and YRD$^{\times}$ (Fig. 3a). Nevertheless, the time-shift of the recordings by YRD$^{\times}$ cause the phase velocities extracted from the retrieved virtual-source responses to exhibit a clear mismatch (Fig. 3d). An additional example, involving the stations HAH$^{\checkmark}$, SKG$^{\checkmark}$ and ISS$^{\times}$, is provided in the supporting material (Fig. S6).

4 AN ADEQUATE MODEL FOR THE DETERMINATION OF INSTRUMENTAL TIMING ERRORS

In this section we introduce a simple model. Using this model, a set of equations can be obtained that will allow us to recover instrumental timing errors. In Sections 6, 7 and 9 we will consider different scenarios for which this system of equations can be solved. Let us denote the arrival time of the medium's direct surface-wave response at positive time, that is, the direct surface-wave in $G\left(\mathbf{x}_j, \mathbf{x}_i, t\right)$, by $t^{(+)}_{i,j}$. Similarly, we denote the arrival time of the direct surface-wave response at negative time, that is, the direct surface-wave in $G\left(\mathbf{x}_j, \mathbf{x}_i, -t\right)$, by $t^{(-)}_{i,j}$. By definition, therefore, $t^{(+)}_{i,j} = -t^{(-)}_{i,j}$. Note that a temporal change in the medium (e.g. Obermann *et al*. 2014) merely modifies the Green's function, which implies that the equality between $t^{(+)}_{i,j}$ and $-t^{(-)}_{i,j}$ will not be affected. Let us now denote a potential instrumental timing error of station S_i by $\delta t^{(\mathrm{ins})}_i$; a positive $\delta t^{(\mathrm{ins})}_i$ implies that v_i represents the vertical particle velocity at a moment later in time than the time t at which it is observed by S_i. Hence, a negative $\delta t^{(\mathrm{ins})}_i$ implies that the recordings by station S_i are subject to a time delay.

Since we consider direct surface-wave responses retrieved through the application of SI [i.e. we exploit relation (2)], we need to introduce a time-shift in the arrival time due to a deviation of the illumination pattern from uniformity: $\delta t^{(\mathrm{src})}_{i,j}$. Because the retrieved direct surface-wave responses at positive and negative time are associated with opposite stationary-phase regions (e.g. Snieder 2004; Boschi & Weemstra 2015), we distinguish between $\delta t^{(+,\mathrm{src})}_{i,j}$ and $\delta t^{(-,\mathrm{src})}_{i,j}$, which represent (illumination related) arrival-time shifts at positive and negative time, respectively (see Fig. 4). These arrival-time shifts can be expected to differ from each other (Weaver *et al*. 2009; Froment *et al*. 2010). Note that the medium appears to be slower for a positive $\delta t^{(+,\mathrm{src})}_{i,j}$, whereas a positive $\delta t^{(-,\mathrm{src})}_{i,j}$ makes the medium appear to be faster than the actual medium. Finally, we account for the presence of spurious energy (introduced in the second paragraph of Section 3) by defining the additional time

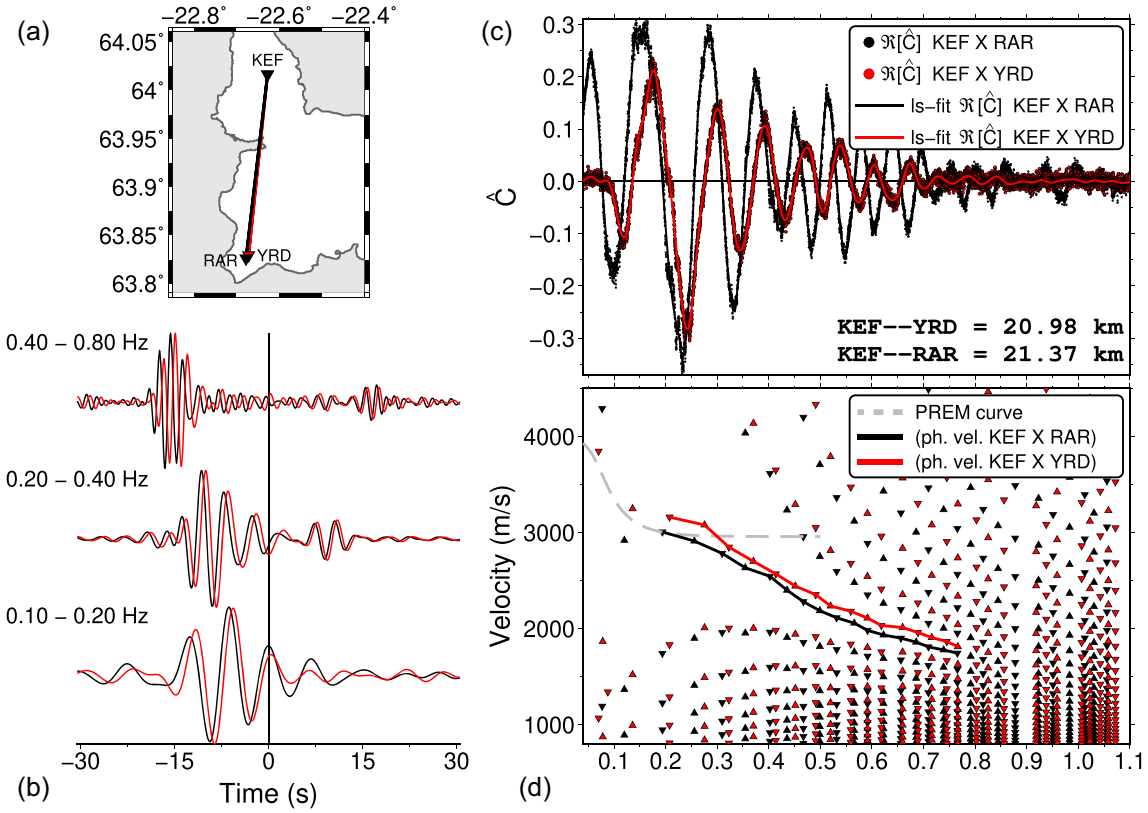

Figure 3. Comparison of the application of SI to the station couples KEF✓–RAR✓ and KEF✓–YRD✗. Stations KEF✓ and RAR✓ are separated by 21.37 km, and stations KEF✓ and YRD✗ are separated by 20.98 km. (a) Station locations and ray paths. (b) The time-averaged cross-correlation is shown for three different frequency bands (time averaged cross-correlation of the recordings by KEF✓ and RAR✓ is depicted as a black solid line; time averaged cross-correlation of the recordings by KEF✓ and YRD✗ is depicted as a red solid line). (c) The real part of the cross-spectrum (dots) with the linear combination of third-order polynomials that best fits their behaviour overlain (solid lines) for both station couples. (d) Velocity values (triangles) for which the zeros of a zeroth order Bessel function of the first kind coincide with the zeros of the least-squares fits in (c) [the procedure is similar to the approach by Ekström *et al*. (2009) and explained in detail in Lindner *et al*. (2018)]. Rayleigh wave fundamental-mode phase velocities for the preliminary reference Earth model (PREM, but with the oceanic layer removed; Dziewonski & Anderson 1981) are given by the gray dashed curve. The PREM dispersion curve is used to determine the seismologically most plausible phase-velocity dispersion curve (black solid curve for station couple KEF✓-RAR✓; red solid curve for station couple KEF✓–YRD✗). For details regarding the picking of these phase-velocity dispersion curves we refer to Kästle *et al*. (2016).

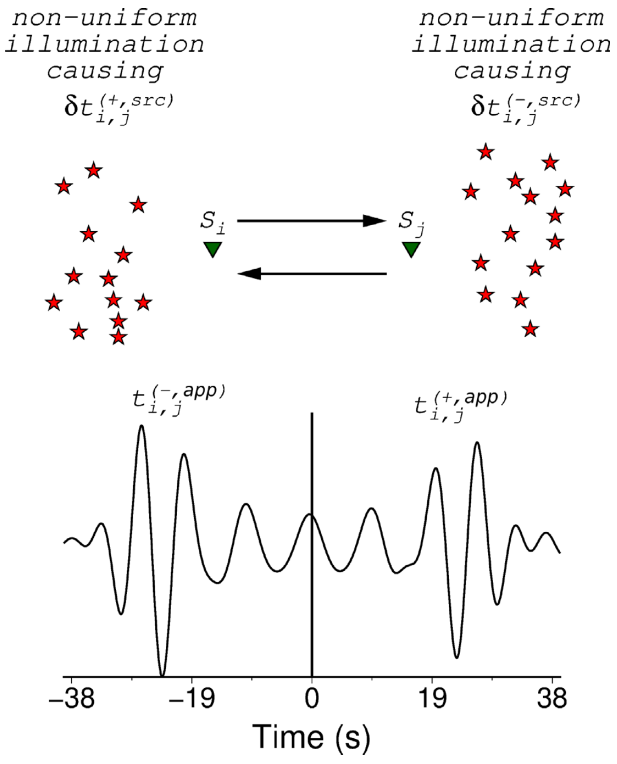

Figure 4. Schematic representation of the illumination related time shifts in the time-averaged cross-correlation.

shifts $\delta t_{i,j}^{(+,\mathrm{spur})}$ and $\delta t_{i,j}^{(-,\mathrm{spur})}$, which, similar to $\delta t_{i,j}^{(+,\mathrm{src})}$ and $\delta t_{i,j}^{(-,\mathrm{src})}$, represent shifts in arrival-time at positive and negative time, respectively. As long as we estimate $C_{i,j}(t)$ by averaging individual $C_{i,j}^{T}(t)$ over finite time, $\delta t_{i,j}^{(+,\mathrm{spur})}$ and $\delta t_{i,j}^{(-,\mathrm{spur})}$ will be non-zero.

Accounting for the time shifts introduced above, the apparent arrival time of the direct response at positive time, denoted by $t_{i,j}^{(+,\mathrm{app})}$, is given by

$$t_{i,j}^{(+,\mathrm{app})} = t_{i,j}^{(+)} + \delta t_i^{(\mathrm{ins})} - \delta t_j^{(\mathrm{ins})} + \delta t_{i,j}^{(+,\mathrm{src})} + \delta t_{i,j}^{(+,\mathrm{spur})}. \tag{3}$$

Similarly, the apparent arrival time of the direct response at negative time, denoted by $t_{i,j}^{(-,\mathrm{app})}$, is given by

$$t_{i,j}^{(-,\mathrm{app})} = t_{i,j}^{(-)} + \delta t_i^{(\mathrm{ins})} - \delta t_j^{(\mathrm{ins})} + \delta t_{i,j}^{(-,\mathrm{src})} + \delta t_{i,j}^{(-,\mathrm{spur})}. \tag{4}$$

Summing the left-hand and right-hand sides of equations (3) and (4), we find

$$t_{i,j}^{(+,\mathrm{app})} + t_{i,j}^{(-,\mathrm{app})} = 2\delta t_i^{(\mathrm{ins})} - 2\delta t_j^{(\mathrm{ins})} + \delta t_{i,j}^{(+,\mathrm{src})} + \delta t_{i,j}^{(-,\mathrm{src})} + \delta t_{i,j}^{(+,\mathrm{spur})} + \delta t_{i,j}^{(-,\mathrm{spur})} \tag{5}$$

In the ideal case that (i) the station couple is illuminated uniformly from all angles, (ii) spurious energy has effectively been stacked out in the time-averaging process and (iii) the recordings by S_i and S_j are not subject to instrumental timing errors, the right-hand side of this equation evaluates to zero and hence $t_{i,j}^{(+,\mathrm{app})} = -t_{i,j}^{(-,\mathrm{app})} = t_{i,j}^{(+)} = -t_{i,j}^{(-)}$.

The left-hand side of eq. (5) is the measurable: in Section 5 we explain how it is inferred from the time-averaged cross-correlations. In case we possess synchronous noise recordings by a total of N seismic stations, a maximum of $N(N-1)/2$ time-averaged cross-correlations can be obtained. We show in Appendix A that the set of equations governing the $t_{i,j}^{(+,\mathrm{app})} + t_{i,j}^{(-,\mathrm{app})}$ can in that case be written as,

$$\mathbf{A}\mathbf{t}^{(\mathrm{ins})} + \mathbf{n}^{(\mathrm{src})} + \mathbf{n}^{(\mathrm{spur})} = \mathbf{t}^{(\mathrm{app})}, \tag{6}$$

where the rows and columns of $\mathbf{A}$ relate to different station pairs and stations, respectively (in this work, both matrices and vectors are indicated in bold; matrices are also capitalized, vectors not). The column vector $\mathbf{t}^{(\mathrm{ins})}$ holds the N instrumental timing errors, and the column vectors $\mathbf{n}^{(\mathrm{src})}$, $\mathbf{n}^{(\mathrm{spur})}$ and $\mathbf{t}^{(\mathrm{app})}$, hold the $\delta t_{i,j}^{(+,\mathrm{src})} + \delta t_{i,j}^{(-,\mathrm{src})}$, $\delta t_{i,j}^{(+,\mathrm{spur})} + \delta t_{i,j}^{(-,\mathrm{spur})}$ and $t_{i,j}^{(+,\mathrm{app})} + t_{i,j}^{(-,\mathrm{app})}$, respectively. Note that the vector $\mathbf{t}^{(\mathrm{app})}$, which contains the measurements, is often referred to as the 'data vector'.

In application to field data, $t^{(+,\mathrm{app})}$ and/or $t^{(-,\mathrm{app})}$ often cannot be determined for all time averaged cross-correlations (i.e. all combinations of i and j). This implies that the number of rows M of the matrix $\mathbf{A}$ (and hence the number of elements of $\mathbf{t}^{(\mathrm{app})}$, $\mathbf{n}^{(\mathrm{src})}$, and $\mathbf{n}^{(\mathrm{spur})}$) will often be smaller than $N(N-1)/2$. The inability to accurately determine $t^{(+,\mathrm{app})}$ and/or $t^{(-,\mathrm{app})}$ can have two reasons. First, in case two stations are too close to each other with respect to the wavelengths considered, the direct surface-wave response at positive time will overlap with the direct surface-wave response at negative time. Second, the absence of sources in one of the two stationary phase directions will prevent the retrieval of the corresponding direct surface-wave response (e.g. Snieder 2004; Boschi & Weemstra 2015). Clearly, this also does not allow determination of the associated arrival time.

In the following section we detail the (automated) procedure for the determination of $t^{(+,\mathrm{app})} + t^{(-,\mathrm{app})}$. In Section 6 we subsequently introduce the ordinary least-squares inversion for the sought-for $\delta t_i^{(\mathrm{ins})}$. In Section 7, the least-squares inversion is augmented with weights that account, to some extent, for the error resulting from deviations from a uniform noise illumination. In that section, and in Section 8, we will also investigate the performance of different inversion strategies and data selection criteria.

5 ESTIMATING $\mathbf{t}_{\mathbf{i,j}}^{(+,\mathbf{app})} + \mathbf{t}_{\mathbf{i,j}}^{(-,\mathbf{app})}$

In application to large-N seismic arrays, the large number of station couples demands the $t^{(+,\mathrm{app})} + t^{(-,\mathrm{app})}$ to be estimated in an automated fashion. For a number of reasons, however, this is far from trivial. First and foremost, without any *a priori* estimate of $\delta t_i^{(\mathrm{ins})}$ and $\delta t_j^{(\mathrm{ins})}$, it is impossible to determine the time window in the time-averaged cross-correlation in which the peaks associated with the two direct surface-wave arrivals should be sought. For example, a large positive $\delta t_i^{(\mathrm{ins})}$ and large negative $\delta t_j^{(\mathrm{ins})}$ could result in a $t_{i,j}^{(+,\mathrm{app})}$ and $t_{i,j}^{(-,\mathrm{app})}$ that are both positive. The fact that it is *a priori* unknown whether the direct surface-waves in $G\left(\mathbf{x}_j, \mathbf{x}_i, t\right)$ and $G\left(\mathbf{x}_j, \mathbf{x}_i, -t\right)$ are both present in the time-averaged cross-correlation, or only one of the two or neither of them, complicates this. Secondly, both the previously mentioned illumination related arrival-time-shift and the arrival-time shifts due to spurious energy hamper the estimation of $t_{i,j}^{(+,\mathrm{app})}$ and $t_{i,j}^{(-,\mathrm{app})}$. Finally, a difference in frequency content of the two direct surface-waves, due to a difference in the power spectrum of sources associated with the two opposite stationary-phase regions, in combination with the dispersive character of the medium, could result in an additional difference between $t_{i,j}^{(+,\mathrm{app})}$ and $-t_{i,j}^{(-,\mathrm{app})}$.

Below, we list the different steps needed to arrive at a proper estimate of $t_{i,j}^{(+,\mathrm{app})} + t_{i,j}^{(-,\mathrm{app})}$. In this process, the just mentioned complexities are overcome by (i) estimating $t_{i,j}^{(+,\mathrm{app})} + t_{i,j}^{(-,\mathrm{app})}$ at once, instead of estimating $t_{i,j}^{(+,\mathrm{app})}$ and $t_{i,j}^{(-,\mathrm{app})}$ separately and (ii) by using *a priori* estimates of the sought-for $\delta t_i^{(\mathrm{ins})}$. How we obtain the *a priori* estimates of the $\delta t_i^{(\mathrm{ins})}$, which we denote by $\delta t_i^{(\mathrm{ins,ap})}$, is explained further below, after we have listed the steps needed to estimate $t_{i,j}^{(+,\mathrm{app})} + t_{i,j}^{(-,\mathrm{app})}$. In order to arrive at a proper estimate of $t_{i,j}^{(+,\mathrm{app})} + t_{i,j}^{(-,\mathrm{app})}$ for each station couple i, j, the receiver–receiver distance $r_{i,j} \equiv |\mathbf{x}_j - \mathbf{x}_i|$ and the reference phase-velocity dispersion curve $c(f)$ are critical. How the reference phase-velocity dispersion curves are obtained, is also detailed after the different steps are listed. The entire process of estimating the $t_{i,j}^{(+,\mathrm{app})} + t_{i,j}^{(-,\mathrm{app})}$ is exemplified in Fig. 5 using the bandpass filtered (0.075–0.225 Hz) time-averaged cross-correlation of station couple O22$^{\boldsymbol{\times}}$–STH$^{\boldsymbol{\times}}$. For each station couple i, j, the steps needed to arrive at a proper estimate of $t_{i,j}^{(+,\mathrm{app})} + t_{i,j}^{(-,\mathrm{app})}$ are:

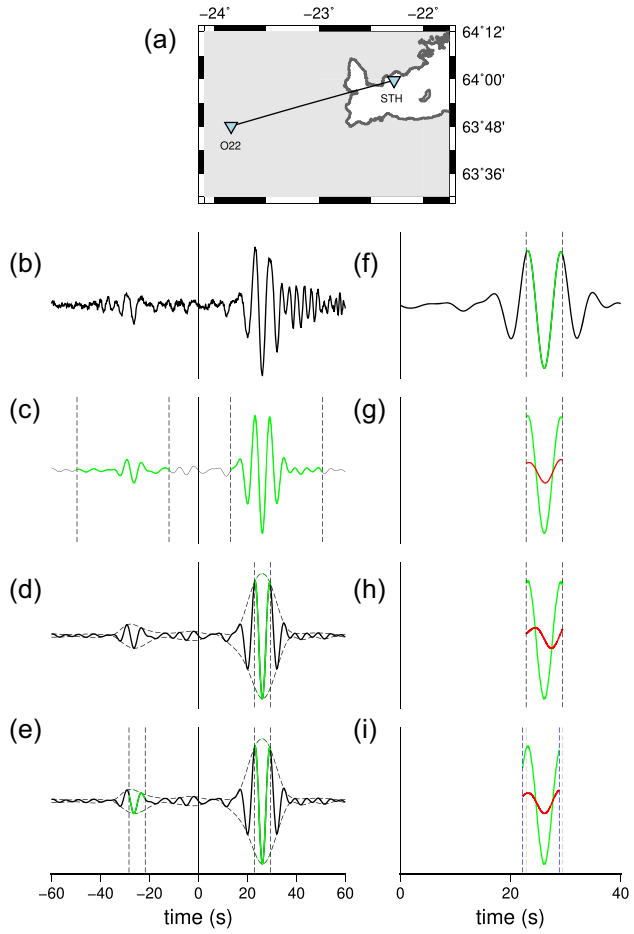

Figure 5. Example of the estimation of $t_{i,j}^{(+,\mathrm{app})} + t_{i,j}^{(-,\mathrm{app})}$. (a) Locations of O22$^{\blacktriangledown}$ and STH$^{\blacktriangledown}$, and the ray path connecting the stations. (b) Time-averaged cross-correlation (we refer to Section 9 for a description of the data processing). (c) Time-averaged cross-correlation bandpass filtered between 0.075 and 0.225 Hz (solid gray line; $f_c = 0.15$ Hz). In the signal windows (start and end times indicated by vertical dashed lines), the bandpass filtered cross-correlation is depicted as a green solid line. (d) Same bandpass filtered cross-correlation as in c (solid black line), but including the peak and trough envelopes (dashed black lines). The window of length $1/f_c$ for which the difference between the peak envelope and trough envelope, averaged over a period of $1/f_c$, attains it maximum, is indicated by vertical dashed lines. The centre of this window is defined as t^{est}. For clarity, the bandpass filtered cross-correlation is depicted as a solid green line in this window. (e) Same as d, but with additionally indicated the window of length $1/f_c$ centred around $2\delta t_i^{(\mathrm{ins,ap})} - 2\delta t_j^{(\mathrm{ins,ap})} - t^{\mathrm{est}}$. (f) Direct surface-wave response at positive time in the window (of length $1/f_c$) centred at t^{est}. (g) Same part of the direct surface-wave response at positive time, but with part of the direct surface-wave response at negative time, folded around $t = 0$, on top of it (red; note that this is not the part of the signal at negative time depicted in green in e because, by folding around $t = 0$, we do not account for the *a priori* estimates $\delta t_i^{(\mathrm{ins,ap})}$ and $\delta t_j^{(\mathrm{ins,ap})}$ of stations O22$^{\blacktriangledown}$ and STH$^{\blacktriangledown}$, respectively). (h) Same as (g), but with the direct surface-wave response at negative time, folded around $t = \delta t_i^{(\mathrm{ins,ap})} - \delta t_j^{(\mathrm{ins,ap})}$ (red; note that this is the part of the signal at negative time depicted in green in e). (i) Windowed response at positive time (green) and windowed response at negative time (red), where the latter is folded around $(t_{i,j}^{(+,\mathrm{app})} + t_{i,j}^{(-,\mathrm{app})})/2$. Note that the windows have been shifted because of the difference in the computed $t_{i,j}^{(+,\mathrm{app})} + t_{i,j}^{(-,\mathrm{app})}$ and $2\delta t_i^{(\mathrm{ins,ap})} - 2\delta t_j^{(\mathrm{ins,ap})}$ (hence the blue vertical dashed lines).

(i) Bandpass filter the time-averaged cross-correlation [i.e. $C_{i,j}(t)$] around the frequency of interest f_c, which is the centre frequency of the pass band (Fig. 5c).

(ii) Based on the receiver–receiver distance $r_{i,j}$ and the reference phase velocity $c(f_c)$ at f_c Hz, compute the station couple's non-dimensional receiver–receiver distance $r_{i,j}^{(\lambda)} \equiv r_{i,j}/\left(c\left(f_c\right)/f_c\right) = f_c r_{i,j}/c(f_c)$, which quantifies the straight line distance between the two station in terms of the number of wavelengths.

(iii) Discard the time-averaged cross-correlation if $r_{i,j}^{(\lambda)} < r^{(\lambda\text{-trh})}$, where $r^{(\lambda\text{-trh})}$ denotes a general, non-dimensional receiver–receiver distance threshold (in terms of wavelengths).

(iv) Determine the *a priori* estimates $\delta t_i^{(\mathrm{ins,ap})}$ and $\delta t_j^{(\mathrm{ins,ap})}$ at f_c Hz and use the station couple's reference surface-wave velocity to determine the time windows in which the direct surface-waves can be expected (the 'signal windows'; see Fig. 5c).

(v) Determine the signal-to-noise ratio (SNR) of the surface-wave arrivals in the signal windows.

(vi) Discard the time-averaged cross-correlation if the SNR of one of the (or both) surface-wave arrivals does not exceed an *a priori* set SNR threshold.

(vii) Compute the peak envelope and the trough envelope of the time-averaged cross-correlation (Fig. 5d).

(viii) Determine the time t^{est} at which the difference between the peak envelope and trough envelope, averaged over a period of $1/f_c$, attains it maximum (depicted green in Fig. 5d). This difference is only computed within the signal windows.
(ix) Interpolate the time-averaged cross-correlation for a time window of length $1/f_c$ centred around t^{est} and a time window of length $1/f_c$ centred around $2\delta t_i^{(\text{ins,ap})} - 2\delta t_j^{(\text{ins,ap})} - t^{\text{est}}$ (depicted green in Fig. 5e) The time window centred around $\min\left(t^{\text{est}}, 2\delta t_i^{(\text{ins,ap})} - 2\delta t_j^{(\text{ins,ap})} - t^{\text{est}}\right)$, that is, the one associated with $G\left(\mathbf{x}_j, \mathbf{x}_i, -t\right)$, we define as window #1. The time window centred around $\max\left(t^{\text{est}}, 2\delta t_i^{(\text{ins,ap})} - 2\delta t_j^{(\text{ins,ap})} - t^{\text{est}}\right)$, that is, the one associated with $G\left(\mathbf{x}_j, \mathbf{x}_i, t\right)$, we define as window #2.
(x) Time reverse the signal in window #1 (the signal in window #2 and the time reverse of the signal in window #1, folded around $t = \delta t_i^{(\text{ins,ap})} - \delta t_j^{(\text{ins,ap})}$, are depicted in Fig. 5h).
(xi) Set the start of both window #1 and window #2 to $t = 0$.
(xii) Cross-correlate the signal in window #1 with the signal in window #2.
(xiii) Between a minimum and maximum time lag of $-1/(2f_c)$ and $1/(2f_c)$, respectively, determine the time lag for which this cross-correlation attains its maximum. This time lag quantifies the deviation of $2\delta t_i^{(\text{ins,ap})} - 2\delta t_j^{(\text{ins,ap})}$ from $t_{i,j}^{(+,\text{app})} + t_{i,j}^{(-,\text{app})}$.
(xiv) Adding the obtained time lag to $2\delta t_i^{(\text{ins,ap})} - 2\delta t_j^{(\text{ins,ap})}$ finally yields the $t_{i,j}^{(+,\text{app})} + t_{i,j}^{(-,\text{app})}$.

A number of steps need some clarification. First, the reference phase-velocity dispersion curve $c(f)$ mentioned in step (ii) is the *a priori* determined velocity dispersion representative of the surface-wave dispersion in the area of interest. If the area over which the seismic stations are distributed is large, multiple reference dispersion curves can be used. At low frequencies (< 0.1 Hz), fundamental-mode velocities for the preliminary reference earth model can be used (PREM; Dziewonski & Anderson 1981). Together with the SNR threshold, the receiver–receiver distance threshold $r^{(\lambda\text{-trh})}$ determines the quality and number of measurements included in the data vector $\mathbf{t}^{(\text{app})}$. In Section 8, we investigate how these thresholds affect the inversion results. Secondly, the *a priori* estimates $\delta t_i^{(\text{ins,ap})}$ (step iv) are in our case determined using relatively low-frequency (0.05 - 0.15 Hz) body- or surface-wave responses to Earthquakes at large distances (recall that we apply our technique to surface-wave arrivals in the 0.1–0.5 Hz range). This is explained below. Third, the SNR in step (v) is defined as the ratio between the maximum absolute amplitude in the signal window and the root-mean-square amplitude of the noise in a time window with a length of 240 s, starting 240 s after $t = \delta t_i^{(\text{ins,ap})} - \delta t_j^{(\text{ins,ap})}$ (significantly later than the slowest expected surface-waves between 0.1 and 0.5 Hz). Fourth, the interpolation in step (ix) is required to ensure that the temporal resolution of $t_{i,j}^{(+,\text{app})} + t_{i,j}^{(-,\text{app})}$ is sufficiently high. Fifth, by limiting the cross-correlation between window #1 and window #2 to maximum absolute time lags of $1/(2f_c)$ (i.e. the maximum of the cross-correlation is sought within a time window of one period), we try to prevent $t_{i,j}^{(+,\text{app})} + t_{i,j}^{(-,\text{app})}$ being off by a value of approximately $1/f_c$, that is, one period. This happening would essentially be similar to what is referred to as cycle skipping in full-waveform inversion (e.g. Warner & Guasch 2014). Finally, we would like to iterate that the code in which the above process is implemented has been made freely available (see Acknowledgements).

The SNR threshold partly determines the number of eligible measurements $t_{i,j}^{(+,\text{app})} + t_{i,j}^{(-,\text{app})}$ (i.e. the length of the data vector $\mathbf{t}^{(\text{app})}$). Consequently, it affects the accuracy of the recovered timing errors. In Section 8, we investigate the effect of the SNR threshold on the accuracy of the recovered timing errors (in combination with the effect of the receiver–receiver distance threshold). We would like to emphasize that the SNR threshold is an independent parameter in our study (and defined in the paragraph above), and that we do not attempt to disentangle the weights of the various factors contributing to the noise or the amplitude of the direct surface-wave. For example, whether a station pair's low SNR is due to relatively high incoherent, station-specific noise or due to the relatively short period of time over which cross-correlations can be averaged (due to a relatively short period of time during which two stations are synchronously recording), is not assessed.

Fig. 6 illustrates the estimation of the $\delta t_i^{(\text{ins,ap})}$. Time-domain application of Fisher's F-statistic (Melton & Bailey 1957; Olson 2004) to the signal recorded by the IMAGE stations yields an estimate of the slowness of the incident Earthquake response. Subsequently, the time shifts on the recordings by the non-IMAGE stations that maximize the Fisher ratio yield the *a priori* estimates $\delta t_i^{(\text{ins,ap})}$. We attribute this estimate to the central frequency of the frequency band of interest (e.g. the $\delta t_i^{(\text{ins,ap})}$ estimated in Fig. 6 we attribute to 0.09 Hz). In Fig. S7, *a priori* estimates of $\delta t_i^{(\text{ins})}$ for all ISOR and SIL stations, and for a range of frequencies, are presented. The *a priori* estimates at these (lower) frequencies are linearly extrapolated to the lowest f_c at which we apply our method. Bringing to mind our reference to cycle skipping above, possessing sufficiently accurate $\delta t_i^{(\text{ins,ap})}$ is analogous to having a sufficiently accurate starting model in full-waveform inversion (e.g. Virieux & Operto 2009).

6 A UNIFORM ILLUMINATION PATTERN

Accurate interferometric Green's function retrieval is contingent on a uniform illumination pattern (Tsai 2009; Wapenaar & Fokkema 2006). Additionally assuming the other conditions associated with eq. (2) to be fulfilled, eq. (6) reduces to,

$$\mathbf{t}^{(\text{app})} = \mathbf{A}\mathbf{t}^{(\text{ins})}. \tag{7}$$

The ordinary least-squares estimator of $\mathbf{t}^{(\text{ins})}$, which we denote by $\tilde{\mathbf{t}}_{(\text{ols})}^{(\text{ins})}$, minimizes the misfit function

$$\chi = \| \mathbf{t}^{(\text{app})} - \mathbf{A}\mathbf{t}^{(\text{ins})} \| . \tag{8}$$

As defined in Section 4 (and written in full in Appendix A), however, the rank of $\mathbf{A}$ is one lower than the number of unknowns N. This indicates that the system of equations is effectively underdetermined (that is, after Gaussian elimination). In practice, this implies that one

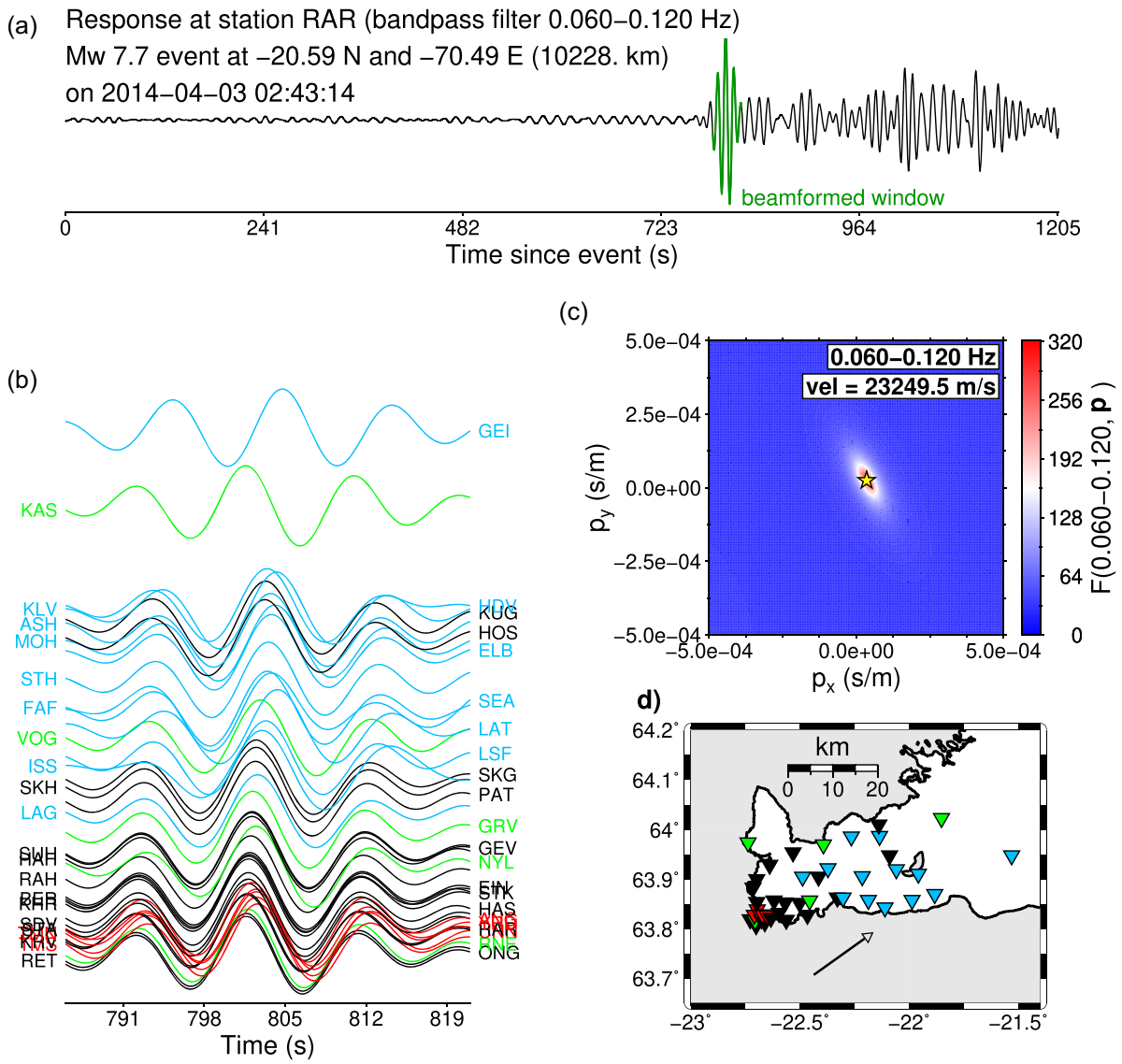

Figure 6. Estimation of the $\delta t_i^{(\mathrm{ins,ap})}$ using a high-magnitude event close to Chile. (a) The near-vertical incident body waves (depicted in green) are bandpass filtered between 0.06 and 0.12 Hz. The response recorded by station RAR✓ is displayed. (b) Zoom of the earthquake's body waves recorded by all online RARR stations. A trace's position along the vertical axis increases proportional to its increase in distance from the earthquake's epicentre. The traces' colours indicate the seismic network/deployment, the station belongs to (see Fig. 1). (c) Best beam resulting from Fisher's *F*-statistic using the IMAGE stations only (Melton & Bailey 1957; Olson 2004). (d) Location of the stations. The arrow indicates the horizontal component of the vector describing the propagation of the body waves indicated in green in (a), as determined by the time-domain Fisher detector.

needs to be certain about the timing of at least one station in order to obtain a unique estimate of $\mathbf{t}^{(\mathrm{ins})}$. In the particular but probable case that that specific station is (or those specific stations are) devoid of timing errors, its (or their) $\delta t_i^{(\mathrm{ins})}$ will coincide with zero. Consequently, its entry (or their entries) can be eliminated from $\mathbf{t}^{(\mathrm{ins})}$. Removing the associated column (or columns) from $\mathbf{A}$, renders the number of unknowns N and the rank of the matrix equal. This applies, for example, to the RARR, of which 30 stations are known to be devoid of timing errors (see Table 1). In the remainder of this work, therefore, the $\delta t_i^{(\mathrm{ins})}$ associated with these 30 stations have been eliminated from the system of equations, rendering the matrix $\mathbf{A}$ full rank. Denoting the transpose of $\mathbf{A}$ by $\mathbf{A}^T$, the estimate of $\mathbf{t}^{(\mathrm{ins})}$ that minimizes χ is then given by (e.g. Snieder & Trampert 1999),

$$\tilde{\mathbf{t}}_{(\mathrm{ols})}^{(\mathrm{ins})} = \left(\mathbf{A}^T\mathbf{A}\right)^{-1}\mathbf{A}^T\mathbf{t}^{(\mathrm{app})}. \tag{9}$$

The absence of a 'noise' vector in eq. (7) implies that the recovered instrumental timing errors will coincide with the actual timing errors, that is, $\tilde{\mathbf{t}}_{(\mathrm{ols})}^{(\mathrm{ins})} = \mathbf{t}^{(\mathrm{ins})}$ (and hence the minimum least-squares error $\tilde{\chi} \equiv \min(\chi) = 0$). By substituting eq. (7) in eq. (9) this becomes explicit: the matrix $\left(\mathbf{A}^T\mathbf{A}\right)^{-1}\mathbf{A}^T\mathbf{A}$, which is often referred to as the resolution matrix (e.g. Snieder & Trampert 1999), coincides with the identity matrix.

Because of the absence of a 'noise' vector in eq. (7) (i.e. both $\mathbf{n}^{(\mathrm{src})}$ and $\mathbf{n}^{(\mathrm{spur})}$ are assumed to be $\mathbf{0}$), eq. (9) recovers the sought-for instrumental timing errors exactly. Only in case individual $C^T_{i,j}(t)$ are averaged over infinite time, however, the ensemble-averaged cross-correlation in eq. (2) can be replaced by the time-averaged cross-correlation (e.g. Hanasoge & Branicki 2013). Since this is in practice unachievable, the time-averaged cross-correlations will always contain some remaining spurious energy (from a model perspective, spurious energy is sometimes referred to as 'realization noise'; Tsai 2011). Consequently, for a uniform illumination pattern,

$$\mathbf{t}^{(\mathrm{app})} = \mathbf{A}\mathbf{t}^{(\mathrm{ins})} + \mathbf{n}^{(\mathrm{spur})} \tag{10}$$

is a more appropriate model. The spurious energy present in the time-averaged cross-correlations, manifested by $\mathbf{n}^{(\mathrm{spur})}$, causes these equations to be inconsistent. The ordinary least-squares solution of the system of equations (10) is given by eq. (9). Substituting the right-hand side of eq. (10) for $\mathbf{t}^{(\mathrm{app})}$ in eq. (9), gives

$$\begin{aligned}\tilde{\mathbf{t}}^{(\mathrm{ins})}_{(\mathrm{ols})} &= \left(\mathbf{A}^T\mathbf{A}\right)^{-1}\mathbf{A}^T\left(\mathbf{A}\mathbf{t}^{(\mathrm{ins})} + \mathbf{n}^{(\mathrm{spur})}\right)\\ &= \mathbf{t}^{(\mathrm{ins})} + \left(\mathbf{A}^T\mathbf{A}\right)^{-1}\mathbf{A}^T\mathbf{n}^{(\mathrm{spur})}.\end{aligned} \tag{11}$$

Clearly, the sought-for instrumental timing errors are not recovered correctly in this case: eq. (11) signifies explicitly that $\tilde{\mathbf{t}}^{(\mathrm{ins})}_{(\mathrm{ols})}$ deviates from $\mathbf{t}^{(\mathrm{ins})}$ due to error propagation (which in turn is due to the presence of spurious energy in the time-averaged cross-correlations). This, in combination with the fact that in application to field data $t^{(+,\mathrm{app})}_{i,j} + t^{(-,\mathrm{app})}_{i,j}$ can often not be determined for all couples i, j, renders it pertinent to consider the variance of the estimator $\tilde{\mathbf{t}}^{(\mathrm{ins})}_{(\mathrm{ols})}$.

Denoting the expected value of a quantity by $E[\,\cdot\,]$, and considering that it is reasonable to assume the expected values of $\delta t^{(+,\mathrm{spur})}_{i,j} + \delta t^{(-,\mathrm{spur})}_{i,j}$ (for any couple i, j) to coincide with zero (Tsai 2011; Weemstra *et al.* 2014), it follows that $E\left[\tilde{\mathbf{t}}^{(\mathrm{ins})}_{(\mathrm{ols})}\right] = \mathbf{t}^{(\mathrm{ins})}$. In addition to the zero mean assumption, let us assume the different elements of $\mathbf{n}^{(\mathrm{spur})}$, that is, the $\delta t^{(+,\mathrm{spur})}_{i,j} + \delta t^{(-,\mathrm{spur})}_{i,j}$, to have coinciding variance σ^2 and be pairwise uncorrelated. Using that the deviation of $\tilde{\mathbf{t}}^{(\mathrm{ins})}_{(\mathrm{ols})}$ from its expected value is given by $\tilde{\mathbf{t}}^{(\mathrm{ins})}_{(\mathrm{ols})} - E\left[\tilde{\mathbf{t}}^{(\mathrm{ins})}_{(\mathrm{ols})}\right]$, the covariance matrix $\mathbf{K}$ is given by,

$$\begin{aligned}\mathbf{K} &\equiv \mathrm{cov}\left[\tilde{\mathbf{t}}^{(\mathrm{ins})}_{(\mathrm{ols})}, \tilde{\mathbf{t}}^{(\mathrm{ins})}_{(\mathrm{ols})}\right]\\ &= E\left[\left(\tilde{\mathbf{t}}^{(\mathrm{ins})}_{(\mathrm{ols})} - E\left[\tilde{\mathbf{t}}^{(\mathrm{ins})}_{(\mathrm{ols})}\right]\right)\left(\tilde{\mathbf{t}}^{(\mathrm{ins})}_{(\mathrm{ols})} - E\left[\tilde{\mathbf{t}}^{(\mathrm{ins})}_{(\mathrm{ols})}\right]\right)^T\right]\\ &= E\left[\left(\left(\mathbf{A}^T\mathbf{A}\right)^{-1}\mathbf{A}^T\mathbf{n}^{(\mathrm{spur})}\right)\left(\left(\mathbf{A}^T\mathbf{A}\right)^{-1}\mathbf{A}^T\mathbf{n}^{(\mathrm{spur})}\right)^T\right]\\ &= \sigma^2\left(\mathbf{A}^T\mathbf{A}\right)^{-1}\end{aligned} \tag{12}$$

where $\sigma^2 \equiv E\left[\left(\delta t^{(+,\mathrm{spur})}_{i,j} + \delta t^{(-,\mathrm{spur})}_{i,j}\right)^2\right]$ and where we used $E\left[\tilde{\mathbf{t}}^{(\mathrm{ins})}_{(\mathrm{ols})}\right] = \mathbf{t}^{(\mathrm{ins})}$ in the first step. The diagonal elements of $\mathbf{K}$ hold the variance of the individual elements of $\tilde{\mathbf{t}}^{(\mathrm{ins})}_{(\mathrm{ols})}$. By denoting the ith element of the vector $\tilde{\mathbf{t}}^{(\mathrm{ins})}_{(\mathrm{ols})}$ by $\tilde{\delta t}^{(\mathrm{ins})}_{i(\mathrm{ols})}$, we therefore have $\mathrm{Var}\left[\tilde{\delta t}^{(\mathrm{ins})}_{i(\mathrm{ols})}\right] = k_{ii}$ (in general, k_{ij} is the element in row i and column j of the matrix $\mathbf{K}$). This implies that the variance of the timing error estimated for the ith station is proportional to the ith element along the diagonal of $\left(\mathbf{A}^T\mathbf{A}\right)^{-1}$. This is because the number of (valid) measurements $t^{(+,\mathrm{app})}_{i,j} + t^{(-,\mathrm{app})}_{i,j}$ contributing to the estimate of that station's timing error is embedded in $\mathbf{A}^T\mathbf{A}$. In other words, timing errors of stations for which only few eligible measurements $t^{(+,\mathrm{app})}_{i,j} + t^{(-,\mathrm{app})}_{i,j}$ are available, will have relatively high variance.

In practice, σ^2 is unknown. An unbiased estimate of σ^2, however, is given by (Rao 1973, section 4a.5),

$$\tilde{\sigma}^2 = \frac{\tilde{\chi}}{M - \mathrm{rk}(\mathbf{A})}, \tag{13}$$

where $\mathrm{rk}(\mathbf{A})$ is the rank of the matrix $\mathbf{A}$, that is the number of unknown instrumental timing errors (N). Recall that M denotes the number of rows of the matrix $\mathbf{A}$, that is the number of (valid) measurements $t^{(+,\mathrm{app})}_{i,j} + t^{(-,\mathrm{app})}_{i,j}$, and $\tilde{\chi} \equiv \min(\chi)$. It is useful to note that eq. (13) follows from the fact that $E[\tilde{\chi}] = [M - \mathrm{rk}(\mathbf{A})]\,\sigma^2$ (Rao 1973). Substituting eq. (13) in eq. (12) allows one to obtain, from the data, an estimate of the variance of recovered timing errors.

We test the inversion for the instrumental timing errors, that is the computation of $\tilde{\mathbf{t}}^{(\mathrm{ins})}_{(\mathrm{ols})}$ in eq. (9), by applying it to synthetic recordings of ambient seismic noise. We consider vertical component particle velocity due to vertical excitation at the Earth's surface. The synthetic ambient noise recordings are generated by placing equally strong, simultaneously acting noise sources every 5000 m along a circle at 15° from the centre of the RARR. Only fundamental-mode surface-waves are considered, and the surface-wave dispersion is computed using the PREM model with an overlying water column of 3 km (Gualtieri *et al.* 2013). We generate four months of one-hour synthetic seismic noise recordings. The recordings by the 30 non-IMAGE stations and the 23 OBSs are given an arbitrary (constant) timing error between –2 and 2 s; the 30 land-based IMAGE stations are free of timing errors. Time-averaged cross-correlations are created by summing the individual hourly cross-correlations. The data processing is equivalent to our processing of the field data, for which we refer to Section 9. The synthetic data contains energy between 0.05 and 0.5 Hz.

We run the inversion for a total of 11 centre frequencies f_c ranging from 0.15 to 0.25 Hz, with increments of 0.01 Hz. A fourth order zero-phase Butterworth filter is applied with a bandwidth of 0.15 Hz. We set the SNR threshold to 10. Because of (i) the uniform illumination,

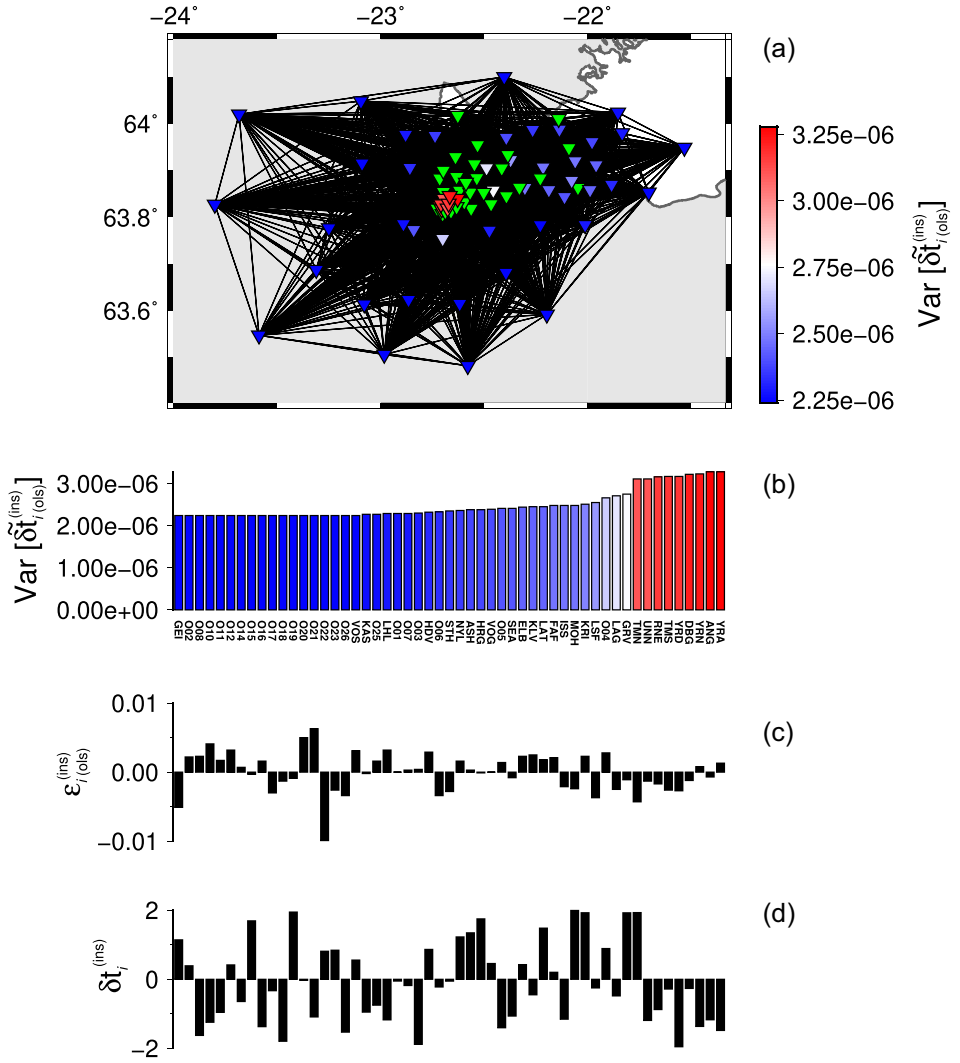

Figure 7. Result of inversion for the 53 modelled (prescribed) instrumental timing error using eq. (9). (a) All eligible station couples are connected with a solid black line. The colours of the stations (inverted triangles) indicate the variance computed according to eq. (12). The 30 land-based IMAGE stations, free of instrumental time shifts, are depicted in green. (b) The variance of the estimated $\delta\tilde{t}^{(\mathrm{ins})}_{i(\mathrm{ols})}$, that is the diagonal terms of $\mathbf{K}$. The stations are sorted in order of increasing variance and the colours of the bars also indicate that variance for compatibility with a (see colour scale). (c) Difference between recovered timing errors and prescribed timing errors (in seconds). (d) Prescribed instrumental timing errors (in seconds). Note that the scale on the vertical axis in (d) is a factor 200 greater than the scale on the vertical axis in (c).

(ii) the total recording period of four months, and (iii) the simple laterally invariable subsurface, the SNR threshold is exceeded for all station couples. Time-averaged cross-correlations of station couples for which the receiver–receiver distance is shorter than one wavelength (i.e. $r^{(\lambda\text{-trh})} = 1$), are discarded. To compute the $r^{(\lambda)}_{i,j}$, we conveniently used the dispersion curve used to model the surface-waves as reference dispersion curve. Due to the decreasing wavelength with increasing frequency, the number of station couples eligible for the estimation of $t^{(+,\mathrm{app})}_{i,j} + t^{(-,\mathrm{app})}_{i,j}$ increases from 2378 at 0.15 Hz to 2778 at 0.25 Hz.

sFor the lowest frequency, $f_c = 0.15$ Hz, the *a priori* estimates $\delta t^{(\mathrm{ins,ap})}_i$ were set to 0 for all stations. The fact that the prescribed $\delta t^{(\mathrm{ins})}_i$ vary between -2 and 2 seconds, however, results in deviations of approximately $1/f_c$ of some of the measured $t^{(+,\mathrm{app})}_{i,j} + t^{(-,\mathrm{app})}_{i,j}$ from the 'correct' $t^{(+,\mathrm{app})}_{i,j} + t^{(-,\mathrm{app})}_{i,j}$. One could interpret these deviations as some sort of cycle skipping, and the fact that they arise underline the importance of sufficiently accurate $\delta t^{(\mathrm{ins,ap})}_i$. By adopting an iterative approach, however, we were able to eliminate them: for a set of monotonically increasing central frequencies $f^{(n)}_c$ ($n = 1, 2, ...$), this iterative approach involves using the $\delta\tilde{t}^{(\mathrm{ins})}_{i(\mathrm{ols})}$ recovered for $f^{(n)}_c$ as the $\delta t^{(\mathrm{ins,ap})}_i$ at $f^{(n+1)}_c$. In our case, $\tilde{\chi}$ reduced from 5386.90 at 0.15 HZ to 2.54 at 0.16 Hz, substantiating the fact that the individual $t^{(+,\mathrm{app})}_{i,j} + t^{(-,\mathrm{app})}_{i,j} - 2\delta\tilde{t}^{(\mathrm{ins})}_i + 2\delta\tilde{t}^{(\mathrm{ins})}_j$ were less than 1 for all eligible station couples at 0.16 Hz. In application to field data, this approach turned out to be particularly useful (Section 9).

Fig. 7 presents the result of the inversion for the 53 prescribed timing errors for $f_c = 0.20$ Hz. To ease the presentation and interpretation of our results, we introduce the residual error $\varepsilon^{(\mathrm{ins})}_{i(\mathrm{ols})} \equiv \delta\tilde{t}^{(\mathrm{ins})}_{i(\mathrm{ols})} - \delta t^{(\mathrm{ins})}_i$. The residual error quantifies the difference between the recovered timing errors and the prescribed timing errors. Note that $\varepsilon^{(\mathrm{ins})}_{i(\mathrm{ols})}$ coincides with the ith element of the vector $\left(\mathbf{A}^T\mathbf{A}\right)^{-1}\mathbf{A}^T\mathbf{n}^{(\mathrm{spur})}$ (see eq. 11). The timing errors remaining after correction (Fig. 7c) are a factor 200 smaller than the prescribed $\delta t^{(\mathrm{ins})}_i$ (Fig. 7d). The maximum residual

error after the inversion has an approximate value of about 0.01 s (station O22$^{\times}$). Considering a surface-wave traveling at 2000 m s^{-1} at 0.2 Hz between two receivers separated by 15 km (one-and-a-half wavelength), this amounts to a phase-velocity error of about 2.6 m s^{-1}. Variances are computed according to eq. (12), with $\tilde{\sigma}^2$ used as a proxy for σ^2 [computed using eq. (13)]. Since $\tilde{\sigma}^2$ is station independent, variations in variances are solely the result of variations in the number of (valid) measurements $t_{i,j}^{(+,\mathrm{app})} + t_{i,j}^{(-,\mathrm{app})}$ contributing to the stations' timing error estimates. The variances on the $\tilde{\delta t}_{i(\mathrm{ols})}^{(\mathrm{ins})}$ predicted for stations in the centre of the array are larger than the variances predicted for stations at the edge of the array. This can be explained by the fact that for station couples including stations in the centre of the array, $r_{i,j}^{(\lambda)}$ less often exceeds $r^{(\lambda\text{-trh})}$, resulting in less eligible $t_{i,j}^{(+,\mathrm{app})} + t_{i,j}^{(-,\mathrm{app})}$ associated with those stations. A final critical note is appropriate: because we assumed the $\delta t_{i,j}^{(+,\mathrm{spur})} + \delta t_{i,j}^{(-,\mathrm{spur})}$ to have coinciding variance σ^2 for all station couples i,j, the estimated variances of the $\tilde{\delta t}_{i(\mathrm{ols})}^{(\mathrm{ins})}$ do not account for variations in SNRs between different station couples. The reason for this is that translating variations in SNR to variations in $\delta t_{i,j}^{(+,\mathrm{spur})}$ (or $\delta t_{i,j}^{(-,\mathrm{spur})}$) is not trivial. Because of decreasing SNRs with increasing receiver–receiver distances (e.g. Tsai 2011; Seats *et al*. 2012), however, one may expect the variance of $\delta t_{i,j}^{(+,\mathrm{spur})} + \delta t_{i,j}^{(-,\mathrm{spur})}$ to increase as a function of receiver–receiver distance. In practice, the just described increase in variance of a recovered timing error for a station located in the centre of the array may therefore be (partly) offset by a decrease in variance of that station's timing error due to a lower average receiver–receiver distance of the couples formed by that station.

7 A NON-UNIFORM ILLUMINATION PATTERN

As explained in Section 3, a non-uniform surface-wave illumination pattern renders the relation between the Green's functions and the time-averaged cross-correlation in eq. (2) inexact. In the model introduced in Section 4, we have accounted for non-uniformities in the illumination pattern through the introduction of $\delta t_{i,j}^{(+,\mathrm{src})}$ and $\delta t_{i,j}^{(-,\mathrm{src})}$. In Appendix A, we therefore introduced the column vector $\mathbf{n}^{(\mathrm{src})}$, such that the set of equations governing the $t_{i,j}^{(+,\mathrm{app})} + t_{i,j}^{(-,\mathrm{app})}$ reads

$$\mathbf{t}^{(\mathrm{app})} = \mathbf{A}\mathbf{t}^{(\mathrm{ins})} + \mathbf{n}^{(\mathrm{src})} + \mathbf{n}^{(\mathrm{spur})}. \tag{6}$$

Weaver *et al*. (2009) use a stationary-phase approximation to derive the error arising from non-uniformities in the illumination pattern, that is they provide expressions for $\delta t_{i,j}^{(+,\mathrm{src})}$ and $\delta t_{i,j}^{(-,\mathrm{src})}$. These authors denote the power of the illuminating wave field by $B(\theta)$, where θ denotes the azimuth measured positive counterclockwise from north. For an arbitrary (but smooth) $B(\theta)$ they find that the arrival-time error on the direct response at positive time, due to the non-uniformity of the illumination pattern, is given by

$$\delta t_{i,j}^{(+,\mathrm{src})} \approx \frac{-B''\left(\theta_{i,j}+180\right)}{8\pi^2 f_c^2\, t_{i,j}\, B\left(\theta_{i,j}+180\right)}. \tag{14}$$

Here, $t_{i,j}$ is the traveltime between $\mathbf{x}_i$ and $\mathbf{x}_j$, and $B''(\theta_{i,j})$ the second derivative of $B(\theta)$ evaluated at $\theta = \theta_{i,j}$. Recall from Section 3 that $\theta_{i,j}$ denotes the azimuth of the vector pointing from $\mathbf{x}_i$ to $\mathbf{x}_j$ (measured counterclockwise from North). Eq. (14) implies that a maximum of $B(\theta)$ at $\theta = \theta_{i,j} + 180$ (i.e. a negative second derivative) results in an arrival time later than the true arrival time, whereas a minimum of $B(\theta)$ at $\theta = \theta_{i,j} + 180$ (i.e. a positive second derivative) results in an arrival time earlier than the true arrival time. Similarly, the illumination related time-shift of the direct response at negative time is given by,

$$\delta t_{i,j}^{(-,\mathrm{src})} \approx \frac{B''\left(\theta_{i,j}\right)}{8\pi^2 f_c^2\, t_{i,j}\, B\left(\theta_{i,j}\right)}. \tag{15}$$

The acoustic derivation by Weaver *et al*. (2009) necessarily assumes (i) sources to be located in the far field, (ii) an interferometric ballistic wave between $\mathbf{x}_i$ and $\mathbf{x}_j$, and (iii) a homogeneous medium. In the context of this work this implies that for expressions (14) and (15) to be exact, the seismic surface-wave noise needs to originate far away from the seismic array of interest and the single-mode surface-waves need to be the result of surface-wave propagation through a laterally invariant subsurface (e.g. Halliday & Curtis 2008). Eqs (14) and (15) imply that if both $B(\theta)$ and $t_{i,j}$ are known, that is, one knows the illumination pattern as well as the traveltime of the direct wave, $\delta t_{i,j}^{(+,\mathrm{src})} + \delta t_{i,j}^{(-,\mathrm{src})}$ could simply be computed. As such, $\mathbf{n}^{(\mathrm{src})}$ could be removed from the right-hand side of (6). In practice, however, $B(\theta)$ and $t_{i,j}$ are not known. Especially obtaining $B(\theta)$ is far from trivial. And in particular for large-N arrays, $B(\theta)$ may vary as a function of location due to variations in the effective surface-wave illumination (e.g. Lin *et al*. 2012). Estimating the average illumination pattern of the array (e.g. Harmon *et al*. 2010) and subsequently computing the $\delta t_{i,j}^{(+,\mathrm{src})}$ and $\delta t_{i,j}^{(-,\mathrm{src})}$ based on the obtained effective $B(\theta)$ may therefore result in significant deviations of the computed $\delta t_{i,j}^{(+,\mathrm{src})}$ and $\delta t_{i,j}^{(-,\mathrm{src})}$ from the actual $\delta t_{i,j}^{(+,\mathrm{src})}$ and $\delta t_{i,j}^{(-,\mathrm{src})}$. For example, in case of USArray data (e.g. Jin & Gaherty 2015), a station couple's illumination at 0.15 Hz in the east of the United States will differ significantly from a station couple's illumination at the same frequency in the centre of the United States. The fact that the ambient noise wave field varies as function of time (e.g. Yang & Ritzwoller 2008; Weemstra *et al*. 2013), in combination with varying recording periods of different seismic stations (often not all stations are recording synchronously; e.g. see Fig. S3), aggravates this. In particular, secondary microseisms have been shown to exhibit significant seasonal variations (Stehly *et al*. 2006). In addition, recordings of stations subject to timing errors cannot be utilized for the estimation of an array specific $B(\theta)$.

As detailed in the paragraph above, it is often practically impossible to obtain a sufficiently good estimate of $B(\theta)$ for the different station couples. The inverse proportionality of the illumination related arrival-time shifts to the traveltime $t_{i,j}$ in equations (14) and (15), however,

suggests that solving eq. (6) in a weighted least-squares sense will yield better estimates of the $\delta t_i^{(\mathrm{ins})}$ than the ordinary least squares solution in eq. (9). The weighted least-squares solution to eq. (6) reads

$$\tilde{\mathbf{t}}_{(\mathrm{wls})}^{(\mathrm{ins})} = \left(\mathbf{A}^T \mathbf{W}_\mathrm{d} \mathbf{A}\right)^{-1} \mathbf{A}^T \mathbf{W}_\mathrm{d} \mathbf{t}^{(\mathrm{app})}. \tag{16}$$

In line with Section 6, we denote the i^{th} element of the vector $\tilde{\mathbf{t}}_{(\mathrm{wls})}^{(\mathrm{ins})}$ by $\tilde{\delta t}_{i(\mathrm{wls})}^{(\mathrm{ins})}$, and introduce the residual error $\varepsilon_{i(\mathrm{wls})}^{(\mathrm{ins})} \equiv \tilde{\delta t}_{i(\mathrm{wls})}^{(\mathrm{ins})} - \delta t_i^{(\mathrm{ins})}$.

The weight matrix $\mathbf{W}_\mathrm{d}$ is a diagonal matrix whose dimension coincides with the number of measurements M. Importantly, the weighted least squares solution (16) is equivalent to the ordinary least squares solution of the system (Snieder & Trampert 1999)

$$\mathbf{W}_\mathrm{d}^{1/2} \mathbf{A} \mathbf{t}^{(\mathrm{ins})} = \mathbf{W}_\mathrm{d}^{1/2} \mathbf{t}^{(\mathrm{app})}, \tag{17}$$

where it should be understood that $\mathbf{W}_\mathrm{d} = \mathbf{W}_\mathrm{d}^{1/2} \mathbf{W}_\mathrm{d}^{1/2}$. Because of the inverse proportionality of the $\delta t_{i,j}^{(+,\mathrm{src})}$ and $\delta t_{i,j}^{(-,\mathrm{src})}$ to the $t_{i,j}$, we define $\mathbf{W}_\mathrm{d}^{1/2}$ directly (instead of $\mathbf{W}_\mathrm{d}$): for each station couple i, j the associated (diagonal) element of $\mathbf{W}_\mathrm{d}^{1/2}$ is ideally given by $t_{i,j}$. Since the $t_{i,j}$ are often also not known, however, we propose to approximate these by the receiver–receiver distances $|\mathbf{x}_j - \mathbf{x}_i|$, which act as a proxy for the $t_{i,j}$. Later in this section, we use synthetic recordings of ambient seismic noise to show that this weighted least-squares inversion yields more accurate estimates of the $\delta t_i^{(\mathrm{ins})}$.

By basing the weight factors in $\mathbf{W}_\mathrm{d}$ on expressions (14) and (15), we have tacitly assumed the elements of $\mathbf{n}^{(\mathrm{src})}$ to be, on average, significantly larger than the spurious arrival-time errors in $\mathbf{n}^{(\mathrm{spur})}$. This is not an unreasonable assumption (e.g. Mulargia 2012; Weemstra *et al*. 2017), in particular because the interferometric surface-wave arrivals need to exceed an *a priori* set SNR threshold (Section 5). Because we ignore the dependence of the $\delta t_{i,j}^{(+,\mathrm{src})} + \delta t_{i,j}^{(-,\mathrm{src})}$ on the factor $B''(\theta)/B(\theta)$, however, assuming their variance to coincide for all station couples is not justified. Consequently, we refrain from estimating the variance on the recovered timing errors in this section.

Although the weighted least-squares solution given in eq. (16) results in more accurate estimates of the instrumental timing errors, improved estimates might be obtained by accounting for the fact that the mean of the illumination related time shifts in $\mathbf{n}^{(\mathrm{src})}$ can be expected to deviate from zero (Tsai 2009; Froment *et al*. 2010). To that end, we define

$$\delta t_{i,j}^{(\mathrm{azi})} \equiv t_{i,j} \left(\delta t_{i,j}^{(+,\mathrm{src})} + \delta t_{i,j}^{(-,\mathrm{src})} \right), \tag{18}$$

which allows us to write $\mathbf{n}^{(\mathrm{src})}$ as

$$\mathbf{n}^{(\mathrm{src})} = \mathbf{f} \odot \mathbf{n}^{(\mathrm{azi})}, \tag{19}$$

where $\odot$ denotes Hadamard matrix multiplication (i.e. element-wise multiplication). The vectors $\mathbf{f}$ and $\mathbf{n}^{(\mathrm{azi})}$ contain the $1/t_{i,j}$ and $\delta t_{i,j}^{(\mathrm{azi})}$, respectively, and are written in full in Appendix B. To account for the fact that the mean of $\mathbf{n}^{(\mathrm{azi})}$ may well not coincide with zero, we write

$$\mathbf{n}^{(\mathrm{azi})} = \mathbf{e}\mu + \mathbf{n}_{(\mathrm{zm})}^{(\mathrm{azi})}, \tag{20}$$

where μ is the mean value of the elements of $\mathbf{n}^{(\mathrm{azi})}$, $\mathbf{e} \equiv (1, 1, \cdots, 1)^T$, and $\mathbf{n}_{(\mathrm{zm})}^{(\mathrm{azi})}$ is a vector with zero mean (hence the subscript 'zm'). Substituting eq. (20) in eq. (19) and inserting it in eq. (6), we have

$$\mathbf{t}^{(\mathrm{app})} = \mathbf{A}\mathbf{t}^{(\mathrm{ins})} + \mathbf{f}\mu + \mathbf{f} \odot \mathbf{n}_{(\mathrm{zm})}^{(\mathrm{azi})} + \mathbf{n}^{(\mathrm{spur})}. \tag{21}$$

To be able to solve this system in a weighted least-squares sense, including the unknown parameter μ, we add this parameter to the vector holding the sought-for instrumental timing errors:

$$\mathbf{t}^{(\mathrm{ins})\prime} \equiv \begin{pmatrix} \mathbf{t}^{(\mathrm{ins})} \\ \mu \end{pmatrix}. \tag{22}$$

Additionally defining

$$\mathbf{A}' \equiv \begin{pmatrix} \mathbf{A} & \mathbf{f} \end{pmatrix} \tag{23}$$

and

$$\mathbf{n}' \equiv \mathbf{f} \odot \mathbf{n}_{(\mathrm{zm})}^{(\mathrm{azi})} + \mathbf{n}^{(\mathrm{spur})}, \tag{24}$$

eq. (21) can be written as

$$\mathbf{t}^{(\mathrm{app})} = \mathbf{A}'\mathbf{t}^{(\mathrm{ins})\prime} + \mathbf{n}'. \tag{25}$$

The weighted least-squares solution to this system of equations reads

$$\tilde{\mathbf{t}}_{(\mathrm{wls})}^{(\mathrm{ins})\prime} = \left(\mathbf{A}'^T \mathbf{W}_\mathrm{d} \mathbf{A}'\right)^{-1} \mathbf{A}'^T \mathbf{W}_\mathrm{d} \mathbf{t}^{(\mathrm{app})}, \tag{26}$$

where the weights are the same as in (16), that is for each station couple i, j the associated (diagonal) element of $\mathbf{W}_\mathrm{d}$ is given by $|\mathbf{x}_j - \mathbf{x}_i|^2$ (as a proxy for the $t_{i,j}^2$). For consistency, we denote the ith element of the vector $\tilde{\mathbf{t}}_{(\mathrm{wls})}^{(\mathrm{ins})\prime}$ by $\tilde{\delta t}_{i(\mathrm{wls})}^{(\mathrm{ins})\prime}$ and introduce the residual error $\varepsilon_{i(\mathrm{wls})}^{(\mathrm{ins})\prime} \equiv \tilde{\delta t}_{i(\mathrm{wls})}^{(\mathrm{ins})\prime} - \delta t_i^{(\mathrm{ins})}$.

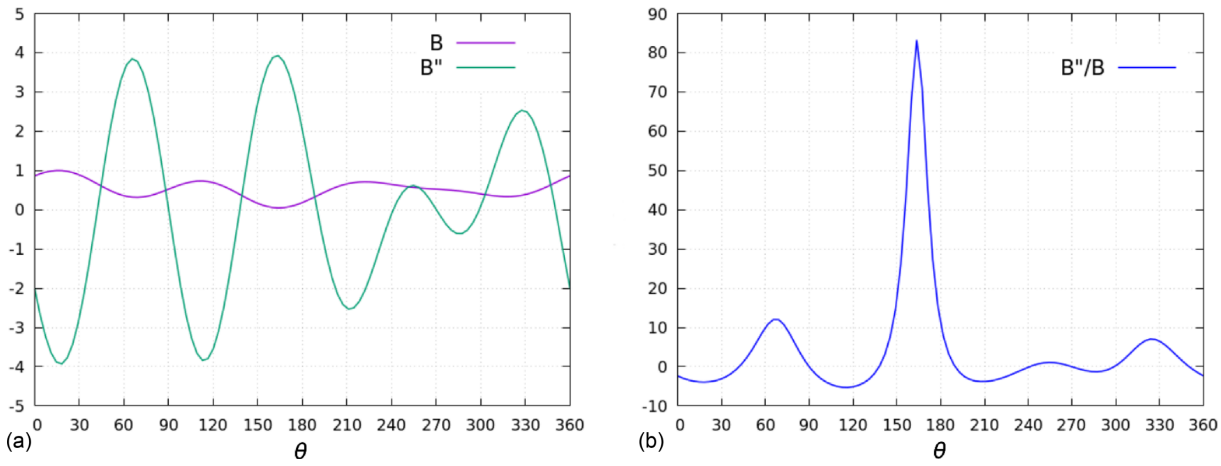

Figure 8. The power of the synthetic surface-wave noise sources illuminating the RARR: $B(\theta) = 1 + 0.25\cos(\theta) + 0.4\cos(3\theta) + 0.25\sin(2\theta) + 0.3\sin(4\theta)$. The sources are placed every 5000 meters along a circle at 15° from the centre of the RARR and θ is measured positive counterclockwise from north. (a) $B(\theta)$ (purple solid line) and its second derivative (green solid line). (b) The factor B''/B which partly predicts the arrival-time error on the direct responses, that is, $\delta t_{i,j}^{(+,\mathrm{src})} + \delta t_{i,j}^{(-,\mathrm{src})}$.

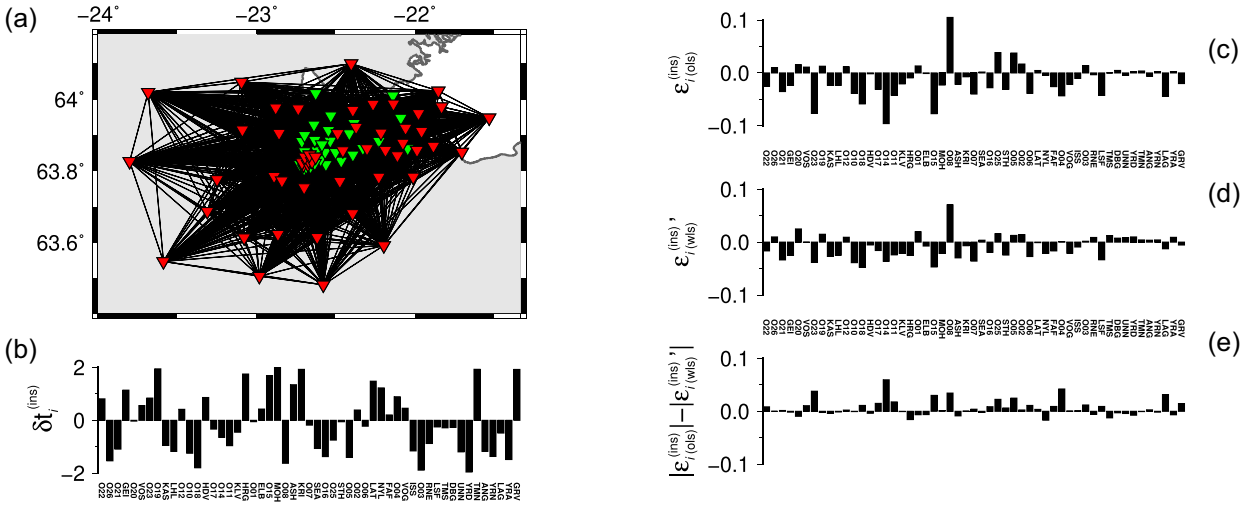

Figure 9. Result of inversion for the 53 modelled (prescribed) instrumental timing errors using eqs (9) and (26). (a) All eligible station couples are connected with a solid black line. The 53 stations with a (prescribed) instrumental timing error are depicted in red. The 30 land-based IMAGE stations, free of instrumental time shifts, are depicted in green. (b) Prescribed instrumental timing errors (same values as Fig. 7d, but ordered differently). (c) Difference between timing errors recovered using the ordinary least-squares inversion (eq. 9) and the prescribed timing errors. (d) Difference between timing errors recovered using the weighted least-squares inversion in eq. (26) and the prescribed timing errors. (e) Absolute residual errors after the ordinary least-squares inversion minus the absolute residual errors after the weighted least-squares inversion. Note that the scale on the vertical axis in (b) is a factor 20 greater than the scale on the vertical axes in (c), (d) and (e). All are in seconds.

We test the weighted least-squares inversions using synthetic recordings of ambient seismic noise. The approach is equivalent to Section 6, but in this case the synthetic ambient surface-wave noise is due to simultaneously acting noise sources of varying power: the power of the sources along the circle at 15° from the centre of the RARR is given by $B(\theta) = 1 + 0.25\cos(\theta) + 0.4\cos(3\theta) + 0.25\sin(2\theta) + 0.3\sin(4\theta)$. In the Fig. 8, we present both $B(\theta)$ and $B''(\theta)$ as well as their ratio, which is an important factor in the expressions derived by Weaver *et al.* (2009) (expressions (14) and (15) above). Again we run the inversion for a total of 11 centre frequencies f_c ranging from 0.15 to 0.25 Hz, with increments of 0.01 Hz and apply a fourth order zero-phase Butterworth filter with a bandwidth of 0.15 Hz.

In Fig. 9, we compare the ordinary least-squares solution given by eq. (9) to the weighted least-squares solution in eq. (26). We compare the solutions for $f_c = 0.20$ Hz with the SNR threshold set to 10 and $r^{(\lambda\text{-trh})}$ set to one. These parameters are the same as the ones used in Section 6. Because of the non-uniform illumination, the SNR threshold is in this case not exceeded for all station couples (although still for many). The residual errors are a factor 20 smaller than the prescribed $\delta t_i^{(\mathrm{ins})}$ (Fig. 9c). The maximum residual error after the ordinary least-squares inversion (station O08$^{\boldsymbol{\times}}$) has an approximate value of about 0.1 s (Fig. 9c). Considering a surface-wave traveling at 2000 m s^{-1} at 0.2 Hz between two receivers separated by 15 km (one-and-a-half wavelength), this amounts to a phase velocity error of about 26 m s^{-1}.

The residual errors associated with the weighted least-squares inversion in eq. (26), that is, the $\varepsilon_{i(\mathrm{wls})}^{(\mathrm{ins})\prime}$, are depicted in Fig. 9(d). Clearly, these residual errors are smaller than the errors remaining after correction by the timing errors obtained through the ordinary least-squares

inversion (Fig. 9c). Specifically, the mean absolute residual error is just under 0.0246 s after the ordinary least-squares inversion, whereas the mean absolute residual error after the weighted least-squares inversion is only about 0.0186 s. Compared to the ordinary least-squares inversion, the weighted least-squared inversion improves the estimates of $\delta t_i^{(\mathrm{ins})}$ therefore by about 25 per cent. The difference between the individual absolute residual errors is presented in Fig. 9(e). In the following section, we (i) investigate the effect of the SNR threshold and $r^{(\lambda\text{-trh})}$ on the inversion results, and (ii) shed some more light on the difference between computing $\tilde{\mathbf{t}}_{(\mathrm{wls})}^{(\mathrm{ins})}$ and computing $\tilde{\mathbf{t}}_{(\mathrm{wls})}^{(\mathrm{ins})\prime}$.

8 DETERMINING THE RECEIVER–RECEIVER DISTANCE AND SNR THRESHOLDS

Using the synthetic recordings from the previous section, we investigate how the different inversion strategies [given by eqs (9), (16), and (26)] perform as a function of $r^{(\lambda\text{-trh})}$ and SNR threshold. We do this by increasing $r^{(\lambda\text{-trh})}$ from 1 to 6, with increments of 0.25 wavelengths, and the SNR threshold from 5 to 60, with increments of 5. Each combination of a specific $r^{(\lambda\text{-trh})}$ and SNR threshold results in a different number of station couples eligible for the estimation of $t_{i,j}^{(+,\mathrm{app})} + t_{i,j}^{(-,\mathrm{app})}$. Obviously, the largest number of eligible station couples (i.e. the combination for which the column vector $\mathbf{t}^{(\mathrm{app})}$ has most elements) is associated with a SNR threshold of 5 and a receiver–receiver distance threshold of 1 wavelength. The results are shown in Fig. 10. Based on our analysis, the following observations can be made. First, for almost all SNR thresholds and $r^{(\lambda\text{-trh})}$, both weighted least-squares inversions decrease the mean absolute residual error by 25 per cent to 30 per cent. Second, large 'jumps' in the mean absolute residual error are sometimes observed between adjacent SNR thresholds and/or adjacent $r^{(\lambda\text{-trh})}$ (manifested by the transitions from blue to red in Figs 10a, b and c). Third, the lowest mean absolute residual errors (indicated by the green boxes) are associated with relatively large $r^{(\lambda\text{-trh})}$. Fourth, the weighted least-squares inversion accounting for deviations from zero of the mean of $\mathbf{n}^{(\mathrm{src})}$ does not necessarily yield lower residual errors than the weighted least-squares solution given by eq. (16). In fact, it appears to perform slightly worse, but we will put this in perspective further below. We discuss these four observations separately in following paragraphs.

Let us first explain the large 'jumps' in the mean absolute residual error observed between some adjacent SNR thresholds and $r^{(\lambda\text{-trh})}$. Similar to the approach for a uniform illumination (Section 6), the *a priori* estimates $\delta t_i^{(\mathrm{ins,ap})}$ were set to zero for all 53 stations at $f_c = 0.15$ Hz. Also, we again used the $\tilde{\delta t}_i^{(\mathrm{ins})}$ recovered for $f_c^{(n)}$ as the $\delta t_i^{(\mathrm{ins,ap})}$ at $f_c^{(n+1)}$ (with $n = 1, 2, ..., 11$; $f_c^{(1)} = 0.15$ Hz). Whereas this approach appears to work well in case the SNR threshold and $r^{(\lambda\text{-trh})}$ are set to relatively low values, this is not the case for either of them being higher (note that the large transitions from blue to red in Figs 10(a)–(c) occur while incrementing to higher SNR thresholds at low $r^{(\lambda\text{-trh})}$, as well as while incrementing to higher receiver–receiver distance thresholds at low SNR thresholds). To explain this, we consider the inversion results for $f_c = 0.20$ Hz associated with a SNR threshold of 25 and $r^{(\lambda\text{-trh})} = 3.25$.

For all three inversion strategies, the mean absolute residual error is significantly higher for a SNR threshold of 25 and $r^{(\lambda\text{-trh})} = 3.25$ than for a SNR threshold of 20 and $r^{(\lambda\text{-trh})} = 3.25$ or a SNR threshold of 25 and $r^{(\lambda\text{-trh})} = 3.0$ (Fig. 10). In this specific case, the difference can be explained by the fact that the recovered instrumental timing errors $\tilde{\delta t}_i^{(\mathrm{ins})}$ of two stations (HRG$^{\boldsymbol{\times}}$ and O03$^{\boldsymbol{\times}}$) turn out to deviate by approximately $1/(2f_c)$ from the prescribed $\delta t_i^{(\mathrm{ins})}$. The reason for this is the low number of stations couples (i.e. the limited length of the vector $\tilde{\mathbf{t}}^{(\mathrm{app})}$) for $f_c = 0.15$ Hz: although 1023 stations couples exceed $r^{(\lambda\text{-trh})} = 3.25$ and a SNR threshold of 25 for $f_c = 0.20$ Hz (Fig. 10f), only 242 station couples exceed the same thresholds for $f_c = 0.15$ Hz. For example, only a single time-averaged cross-correlation involving station O03$^{\boldsymbol{\times}}$ exceeds those thresholds at that central frequency. Due to the lack of sufficiently accurate $\delta t_i^{(\mathrm{ins,ap})}$ at 0.15 Hz ($\delta t_i^{(\mathrm{ins,ap})} = 0$), the $t_{i,j}^{(+,\mathrm{app})} + t_{i,j}^{(-,\mathrm{app})}$ estimated for that specific station couple deviates by about one period ($1/f_c$) from the 'correct' $t_{i,j}^{(+,\mathrm{app})} + t_{i,j}^{(-,\mathrm{app})}$. This results in $\tilde{\delta t}_i^{(\mathrm{ins})}$ deviating by about $1/2f_c$ from the prescribed $\delta t_i^{(\mathrm{ins})}$. And because $\tilde{\delta t}_i^{(\mathrm{ins})}$ recovered for $f_c = 0.15$ Hz serves as the $\delta t_i^{(\mathrm{ins,ap})}$ for $f_c = 0.16$ Hz, the $\tilde{\delta t}_i^{(\mathrm{ins})}$ recovered for $f_c = 0.16$ Hz as the $\delta t_i^{(\mathrm{ins,ap})}$ for $f_c = 0.17$ Hz, and so forth, this error propagates while incrementing to higher frequencies. (In the supporting material, we display the difference between the $t_{i,j}^{(+,\mathrm{app})} + t_{i,j}^{(-,\mathrm{app})}$ (i.e. the measurements) and the $2\tilde{\delta t}_i^{(\mathrm{ins})} - 2\tilde{\delta t}_j^{(\mathrm{ins})}$ at $f_c = 0.20$ Hz. Differences are shown for a SNR threshold of 25 and $r^{(\lambda\text{-trh})} = 3$ (Fig. S8), and a SNR threshold of 25 and $r^{(\lambda\text{-trh})} = 3.25$ (Fig. S9)). In case of lower thresholds, more station couples (measurements) contribute to the estimation of the stations' $\delta t_i^{(\mathrm{ins})}$ at the lowest central frequency, which prevents this from happening. Consequently, this example underlines the importance of sufficiently accurate $\delta t_i^{(\mathrm{ins,ap})}$.

The 25–30 per cent decrease of the mean absolute residual error while using the weighted least-squares inversions, instead of the ordinary least-squares inversion, is fairly constant across SNR thresholds and receiver–receiver separation thresholds. The benefit of the weighted least-squares inversion appears to be somewhat higher for lower SNR thresholds and lower $r^{(\lambda\text{-trh})}$ (Fig. 10d). The difference is relatively small though, especially if one ignores the combinations of SNR thresholds and $r^{(\lambda\text{-trh})}$ for which the mean absolute residual error suddenly increases (i.e. combinations associated with red coloured boxes in Figs 10(a)–(c). Because of the predicted inverse proportionality of $\delta t_{i,j}^{(+,\mathrm{src})}$ and $\delta t_{i,j}^{(-,\mathrm{src})}$ to $t_{i,j}$ [eqs (14) and (15), respectively], one would expect the benefit from the weighted least-squares inversion to be higher for lower $r^{(\lambda\text{-trh})}$. The fact that eqs (14) and (15) do not predict $\delta t_{i,j}^{(+,\mathrm{src})}$ and $\delta t_{i,j}^{(-,\mathrm{src})}$ very well for receiver–receiver separations of one to two wavelengths, however, is probably the reason that this is not the case. This can be attributed to the stationary-phase approximation that is used to derive eqs (14) and (15) (Weaver *et al*. 2009). Consequently, there is a receiver–receiver distance below which the predictive quality of these two equations deteriorates and hence the weights in (16) become less adequate. At the same time, however, the 25–30 per cent improvement indicates that this receiver–receiver distance is lower than the aperture of the RARR.

The low residual errors indicated by the green boxes in Fig. 10 are associated with relatively large $r^{(\lambda\text{-trh})}$. The difference between these mean absolute residual errors and many of the mean absolute residual errors associated with other $r^{(\lambda\text{-trh})}$ and/or SNR thresholds, however, is minimal. Moreover, the number of stations for which $\tilde{\delta t}_i^{(\mathrm{ins})}$ are obtained, decreases for higher thresholds. This is a direct consequence of the decrease in the number of station couples exceeding higher $r^{(\lambda\text{-trh})}$ and/or higher SNR thresholds (Fig. 10f), which implies that some of

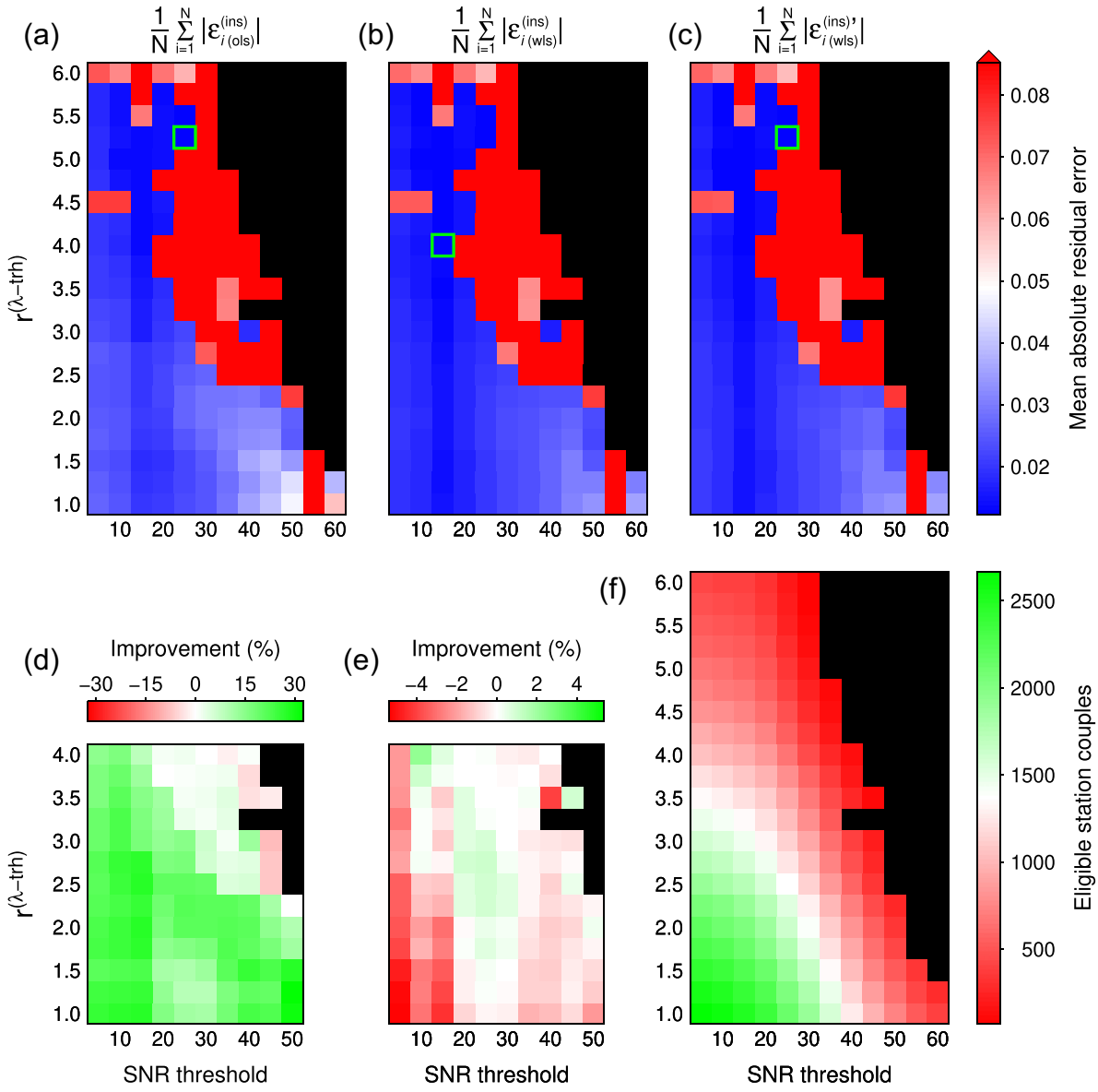

Figure 10. Performance of the ordinary least-squares inversion (eq. 9) and the two weighted least-squares inversions (eqs 16 and (26) as a function of the SNR threshold (horizontal axis) and the non-dimensional receiver–receiver distance threshold $r^{(\lambda\text{-trh})}$ (vertical axis). The inversions are evaluated using time-averaged cross-correlations bandpass filtered between 0.125 and 0.275 Hz ($f_c = 0.20$ Hz). The wavelength is estimated using the reference phase-velocity dispersion curves (see Section 5). (a) Mean absolute residual error after the ordinary least-squares inversion. (b) Mean absolute residual error after the weighted least-squares solution given by eq. (16). (c) Mean absolute residual error after the weighted least-squares solution given by eq. (26). In all cases, the $r^{(\lambda\text{-trh})}$ and SNR threshold associated with the the minimum mean absolute residual error is marked by means of a green box. (d) Decrease (in percentages) of the mean absolute residual error, in case the weighted-least squares solution given by eq. (16) is computed instead of the ordinary least-squares solution. (e) Decrease (percentages) of the mean absolute residual error, in case the weighted-least squares solution given by eq. (26) is computed instead of the weighted-least squares solution given by eq. (16). Black boxes indicate that for that SNR threshold and receiver–receiver distance threshold the number of unknowns N exceeds the rank of $\mathbf{A}$. (f) Number of station couples for which both direct arrivals in the time-averaged cross-correlation exceed the SNR threshold, and for which the $r_{i,j}^{(\lambda)}$ exceed $r^{(\lambda\text{-trh})}$.

the stations are simply not included in $\tilde{\mathbf{t}}_{(\text{wls})}^{(\text{ins})\prime}$. This is also the reason that we only show the relative improvement of the weighted least-squares approaches up to receiver–receiver distance thresholds of four wavelengths in Figs 10(d) and (e). Note that we did not set an additional threshold in the sense that each station should have at least so many time-averaged cross-correlations contributing to the inversion, that is, that it should be associated with a minimum number of elements in $\mathbf{t}^{(\text{app})}$. We did a test where we set that number to three, but it did not improve the estimated $\delta t_i^{(\text{ins})}$, whereas it did cause a (small) drop in the number of stations for which $\tilde{\delta t}_i^{(\text{ins})}$ were obtained. In that context, it is useful to note that the SNR thresholds and $r^{(\lambda\text{-trh})}$ for which no inversion results are reported (coloured black in Fig. 10) rendered the rank of $\mathbf{A}$ lower than the number of unknowns, that is lower than the number of elements in $\mathbf{t}^{(\text{ins})}$ (or $\mathbf{t}^{(\text{ins})\prime}$). The cause for this rank deficiency is the lack of a 'connection' between two (or more) sets of stations. That is, because the number of eligible station couples is relatively low for those receiver–receiver distance thresholds and SNR thresholds (see Fig. 10f), the system of equations is associated with two (or

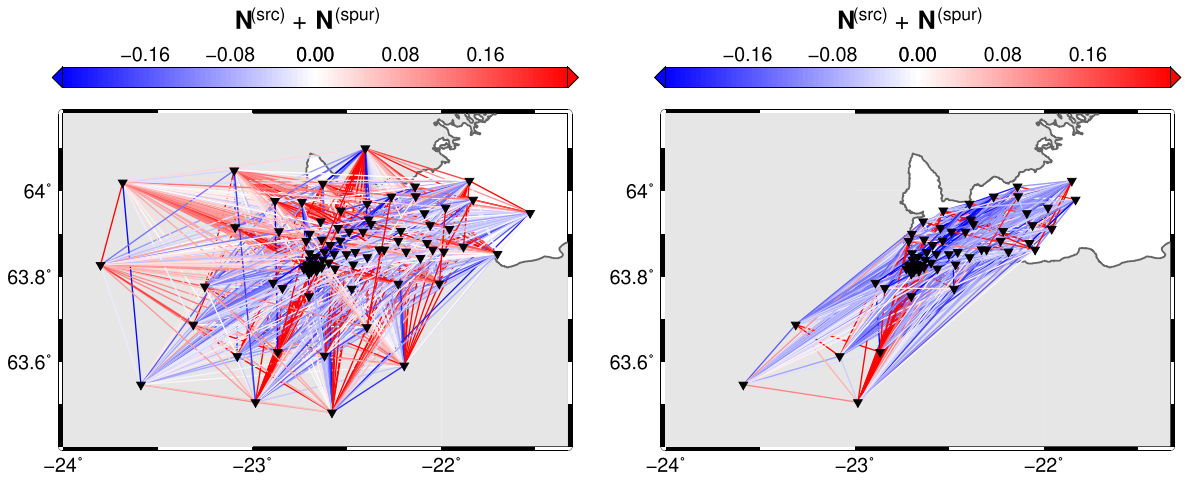

Figure 11. Ray representation of $\delta t_{i,j}^{(+,\mathrm{src})} + \delta t_{i,j}^{(-,\mathrm{src})} + \delta t_{i,j}^{(+,\mathrm{spur})} + \delta t_{i,j}^{(-,\mathrm{spur})}$ (obtained through computation of $t_{i,j}^{(+,\mathrm{app})} + t_{i,j}^{(-,\mathrm{app})} - 2\delta t_i^{(\mathrm{ins})} + 2\delta t_j^{(\mathrm{ins})}$) for the RARR (left-hand panel) as well as for an arbitrary subset of the RARR (right-hand panel). These specific values are associated with a SNR threshold of 10, and a receiver–receiver distance threshold of 1.5 wavelengths. For all station pairs i, j, we defined stations i and j such that $\theta_{i,j} < 180$.

more) separate groups of stations lacking a common time-averaged cross-correlation. Effectively, one therefore has two separate systems of equations. Although we did not attempt this, one could of course run the inversions for these systems of equations separately (provided each of them contains at least one station devoid of a timing error).

The results in Fig. 10 suggest that the weighted least-squares solution given by eq. (26) does not yield more accurate $\tilde{\delta t}_i^{(\mathrm{ins})}$ than the weighted least-squares solution given by eq. (16). In fact, the mean absolute residual error appears to be slightly higher (Fig. 10e). Our synthetic test, however, considers only one specific illumination pattern and one specific array geometry (namely, that of the RARR). That is, one has to be careful drawing general conclusions based on the results presented in Fig. 10. Consider for example the factor B''/B that determines the azimuthal dependence of $\delta t_{i,j}^{(+,\mathrm{src})}$ and $\delta t_{i,j}^{(-,\mathrm{src})}$ on the power of the incident noise field [see eqs (14) and (15)]: in Fig. 8(b) we see that for the prescribed illumination pattern this factor may result in both positive and negative $\delta t_{i,j}^{(+,\mathrm{src})}$ and $\delta t_{i,j}^{(-,\mathrm{src})}$. In other words, it depends on the array geometry (i.e. the $\theta_{i,j}$) relative to the illumination pattern [i.e. $B(\theta)$] whether computing $\tilde{\mathbf{t}}_{(\mathrm{wls})}^{(\mathrm{ins})\prime}$ yields an advantage.

In Fig. 11 we present $\delta t_{i,j}^{(+,\mathrm{src})} + \delta t_{i,j}^{(-,\mathrm{src})} + \delta t_{i,j}^{(+,\mathrm{spur})} + \delta t_{i,j}^{(-,\mathrm{spur})}$ for each eligible station couple. This is obtained through computation of $t_{i,j}^{(+,\mathrm{app})} + t_{i,j}^{(-,\mathrm{app})} - 2\delta t_i^{(\mathrm{ins})} + 2\delta t_j^{(\mathrm{ins})}$, which, of course, is only possible because the $\delta t_i^{(\mathrm{ins})}$ are known for the synthetic data. For each station couple i, j presented in Fig. 11 we computed the time-averaged cross-correlation such that $\theta_{i,j} < 180$. Consequently, from eq. (14) it follows that the $\delta t_{i,j}^{(+,\mathrm{src})}$ depend, for all station couples, on values of $-B''/B$ between 180° and 360°. Similarly, the sign of $\delta t_{i,j}^{(-,\mathrm{src})}$ depends for all stations couples on the sign of B''/B for $\theta_{i,j} < 180$ (see eq. 15). As the left-hand map in Fig. 11 already suggests, we find that the mean of $\mathbf{n}^{(\mathrm{src})} + \mathbf{n}^{(\mathrm{spur})}$ is (perhaps coincidentally) relatively close to zero. This explains the lack of improvement in Fig. 10(e). By considering only a subset of the RARR stations, however, we demonstrate that the inversion associated with eq. (26) certainly has its merits.

In Fig. 12, the performances of the ordinary least-squares inversion and the two weighted least-squares inversions are again compared for different $r^{(\lambda\text{-trh})}$ and SNR thresholds. These inversion results, however, are associated with the subset of stations presented on the right map in Fig. 11. Just as for our analysis above (Fig. 10), the inversions are run using $t_{i,j}^{(+,\mathrm{app})} + t_{i,j}^{(-,\mathrm{app})}$ estimated from time-averaged cross-correlations filtered between 0.125 and 0.275 Hz ($f_c = 0.20$ Hz). We now only evaluate $r^{(\lambda\text{-trh})}$ up to 2.5 and the SNR threshold up to 30. In this case the mean of $\mathbf{n}^{(\mathrm{src})} + \mathbf{n}^{(\mathrm{spur})}$ turns out to deviate more from zero. Consequently, the mean absolute residual error decreases up to 14 per cent in case $\tilde{\mathbf{t}}_{(\mathrm{wls})}^{(\mathrm{ins})\prime}$ is computed instead of $\tilde{\mathbf{t}}_{(\mathrm{wls})}^{(\mathrm{ins})}$, showing the advantage of the former inversion approach.

9 APPLICATION TO FIELD DATA

In this section, we present the application of the weighted least-squares inversion in eq. (26) to the time-averaged cross-correlations of the RARR. Our analysis is restricted to time-averaged cross-correlations of continuous recordings of vertical particle velocity. This is similar to the application on synthetic data. It is useful to note, however, that also horizontal component data could be included in the inversion. In particular because the interferometric surface-wave responses retrieved in this study are due to Rayleigh waves. These Rayleigh waves also have a so-called radial component (Aki & Richards 2002), which may equally well be used to retrieve surface-wave responses and phase velocity dispersion (e.g. Kimman *et al*. 2012). Because the noise on the vertical component receiver–receiver cross-correlation will at best only be partially correlated with the noise on the radial component receiver–receiver cross-correlation (e.g. van Wijk *et al*. 2011), adding the radial component time-averaged cross-correlations to the set of equations would probably yield more accurate estimates of the timing errors.

The following processing has been applied to obtain the time-averaged cross-correlations:

(i) Decimate recordings to 25 samples per seconds.
(ii) Remove theoretical instrument response (see also Section 2).

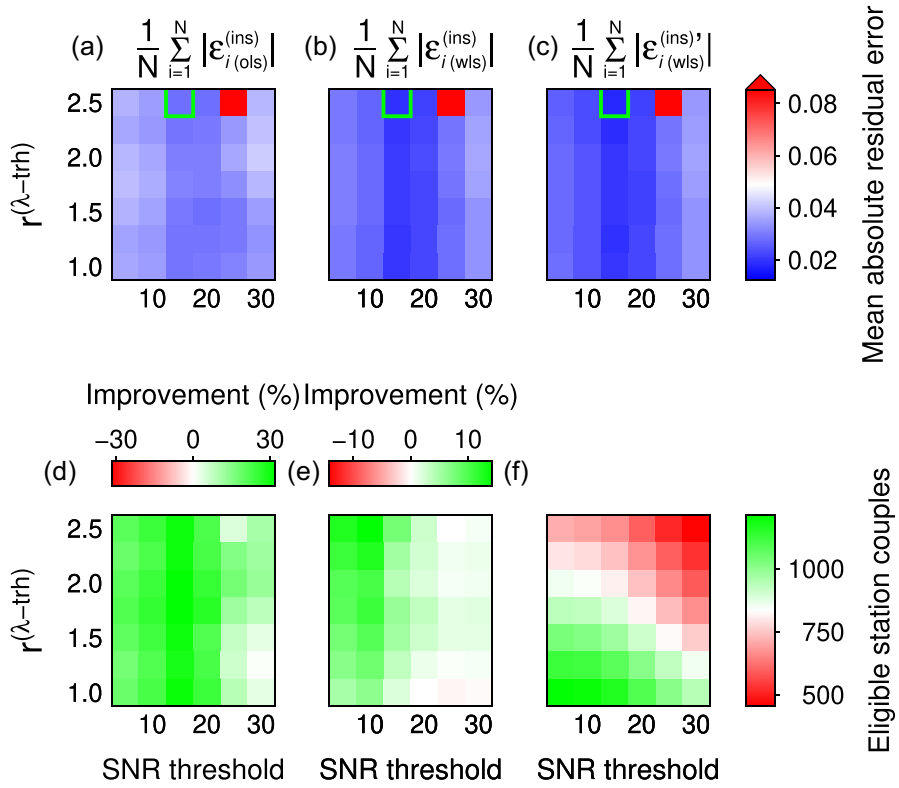

Figure 12. Same as Fig. 10, but for the station configuration depicted on the right map in Fig. 11. For the mean absolute residual error, we used the same colour scale as in Fig. 10.

(iii) Cut available data in windows of one hour with 50 per cent overlap.
(iv) Detrend, taper, zero pad (with one hour of zeros) and Fourier transform the resulting two-hour time series.
(v) Spectral normalization of each frequency sample by average spectral amplitude in a frequency band of 0.005 Hz (36 pts) surrounding that frequency.
(vi) Cross-correlate individual recordings, yielding individual cross-correlations with a length of 2 hr.
(vii) For each station couple, compute the time-average of the individual cross-correlations (sum of the cross-correlations associated with the individual windows, divided by the number of windows).
(viii) Discard time-averaged cross-correlations computed from less than 75 d of synchronous recordings (without gaps).

A few steps need some clarification. First, the 50 per cent overlap is simply implemented to increase SNRs (e.g. Seats *et al*. 2012; Weemstra *et al*. 2013). Second, besides whitening of the spectrum, spectral normalization effectively causes each individual 2-hr cross-correlation to weight equally in the final time-averaged cross-correlation. Third, time-averaged cross-correlations computed from less than 75 d of synchronous recordings are discarded because they can be expected to (i) have a too low SNR and (ii) to be prone to relatively large illumination related time shifts. Finally, the recordings by two stations, O05✗ and O12✗, do not share a synchronous recording period exceeding 75 d with any of the other stations. (see Fig. S1). Consequently, no instrumental timing errors can and will be estimated for these two stations.

We run the inversion for a total of 63 centre frequencies f_c ranging from 0.13 to 0.75 Hz, with increments of 0.01 Hz. A fourth order zero-phase Butterworth filter is applied, whose bandwidth increases from 1.2 octave at 0.13 Hz to 0.8 octave at 0.75 Hz (note that 1.2 octave at 0.13 Hz yields a narrower bandwidth than 0.8 octave at 0.75 Hz). This approach is adopted to ensure that the time-averaged cross-correlations do not have a too monochromatic character at higher frequencies, that is, close to 0.75 Hz, but, at the same time, still allow timing errors representative for the central frequency concerned to be estimated. We set the SNR threshold to 15 and $r^{(\lambda\text{-trh})}$ to 1.5. The $r_{i,j}^{(\lambda)}$ are in this case computed using the surface-wave velocity between stations KEF✓ and ONG✓ (both IMAGE stations) as reference phase velocity (see Section 5). Bearing in mind our discussion in the previous section, an additional threshold was set in the sense that each station should have at least three time-averaged cross-correlations contributing to the inversion, that is, that it should be associated with a minimum of three elements in $\mathbf{t}^{(app)}$. The *a priori* estimates $\delta t_i^{(ins,ap)}$ are determined using relatively low-frequency (0.05–0.15 Hz) body- or surface-wave responses to Earthquakes at large distances. This process is described in detail in Section 5, and the results for the ISOR, SIL, and REYKJANET stations are depicted in Fig. S7. These are linearly extrapolated to obtain the $\delta t_i^{(ins,ap)}$ at $f_c = 0.13$ Hz for those stations; for the OBSs, the $\delta t_i^{(ins,ap)}$ are set to zero at 0.13 Hz. Just as for the synthetic data, we used the $\tilde{\delta t}_{i(wls)}^{(ins)\prime}$ recovered for $f_c^{(n)}$ as the $\delta t_i^{(ins,ap)}$ at $f_c^{(n+1)}$ (with $n = 1, 2, ..., 63$; $f_c^{(1)} = 0.13$ Hz).

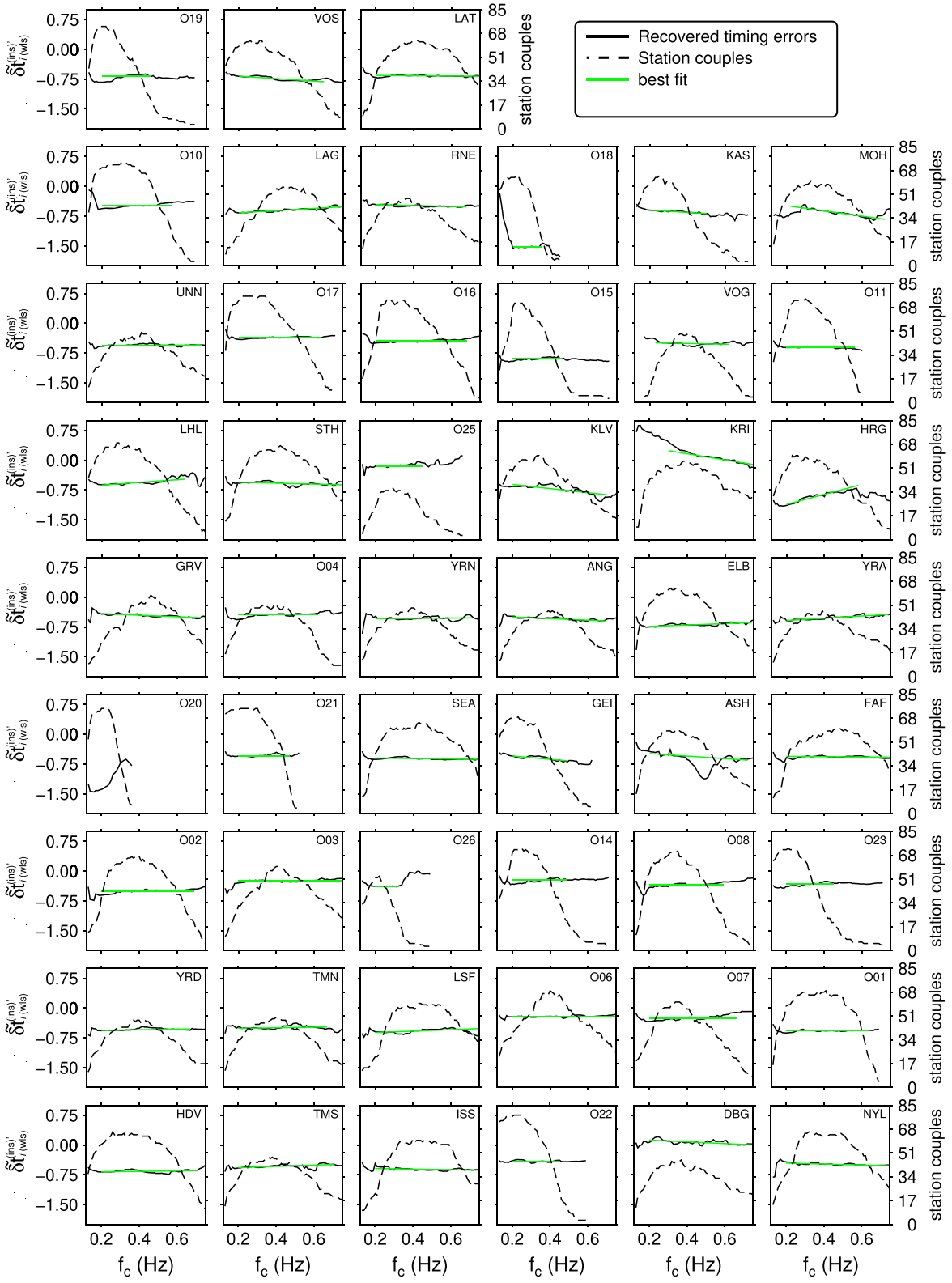

Figure 13. Timing errors recovered using the weighted least-squares inversion in eq. (26). Solid black lines depict the $\tilde{\delta}t^{(\mathrm{ins})\prime}_{i(\mathrm{wls})}$ (in seconds). The dashed black lines indicate, as a function of frequency, the number of station couples formed by the station concerned. Green solid lines indicate the best fitting models.

In Fig. 13, the $\tilde{\delta}t^{(\mathrm{ins})\prime}_{i(\mathrm{wls})}$ are given as a function of frequency. The total number of station couples M eligible for the estimation of $t^{(+,\mathrm{app})}_{i,j} + t^{(-,\mathrm{app})}_{i,j}$ increases from 587 at 0.13 Hz to around 1900 at 0.35 Hz, but then decreases down to about 500 at 0.75 Hz. The initial increase is predominantly due to the decreasing wavelength with increasing frequency, whereas the decrease of the number of station couples

beyond 0.35 Hz is due to rapidly decreasing SNRs. As one would expect from the observation that the overall number of eligible station couples decreases beyond 0.35 Hz, individual stations are associated with fewer time-averaged cross-correlations beyond that frequency (dashed black lines). For most stations we observe that the recovered timing errors are rather stable beyond 0.2 Hz, whereas a 'correction' of the recovered timing errors can be observed while transitioning from 0.13 to about 0.20 Hz. We attribute this 'correction' to the increasing number of eligible station station couples in combination with the effect of the *a priori* estimates $\delta t_i^{(\mathrm{ins,ap})}$ becoming more accurate. The latter effectively reduces the number of measurements $t_{i,j}^{(+,\mathrm{app})} + t_{i,j}^{(-,\mathrm{app})}$ that deviate by approximately one period, that is, $1/f_c$, from the 'correct' value. Something we also observed in our numerical experiments in Sections 6 and 7.

Although, for most stations, the recovered timing errors are rather stable above 0.2 Hz, we do observe some fluctuations of the recovered timing errors, in particular at frequencies marked by a decline in the number of station couples for the station concerned. In essence, this can be explained by the fact that a lower number of measurements, that is, $t_{i,j}^{(+,\mathrm{app})} + t_{i,j}^{(-,\mathrm{app})}$, simply results in a less constrained model. One should additionally bear in mind that the microseisms, which constitute the ambient seismic surface-wave field, have a spatial excitation pattern that generally varies as a function of frequency (e.g. Bromirski *et al*. 2005; Gualtieri *et al*. 2013). Consequently, the effective surface-wave illumination of the RARR most likely varies as a function of frequency in the frequency range of interest here, causing additional frequency-dependent fluctuations. This implies that weighting individual measurements proportional to their receiver–receiver separation does not entirely remove the effect of the illumination pattern on the recovered timing errors. Since the factor B''/B is probably even more important (see eqs 14 and 15), this should not come as a surprise.

For each station, we display a 'best fit' to the recovered timing errors in Fig. 13. For that purpose, we used two different models. For the OBSs we assume the timing errors to be frequency independent, because we assume these errors to be solely due to clock drift (these stations are equipped with broadband instruments). The timing errors of the stations of the SIL, REYKJANET and ISOR networks are fit with a linear model, which we expect to be adequate for the relatively narrow frequency range considered here. In both cases, we (i) only take into account $\tilde{\delta t}_{i(\mathrm{wls})}^{(\mathrm{ins})\prime}$ associated with central frequencies f_c for which the number of station couples exceed 20, (ii) require all $\tilde{\delta t}_{i(\mathrm{wls})}^{(\mathrm{ins})\prime}$ to be within 0.25 s from the best fitting model and (iii) require a minimum of ten $\tilde{\delta t}_{i(\mathrm{wls})}^{(\mathrm{ins})\prime}$ to meet the two previous criteria. Station O20✗, for example, does not fulfil the third condition, preventing a final model to be obtained for this station. Because of the aforementioned 'correction' below 0.2 Hz, we only use $\tilde{\delta t}_{i(\mathrm{wls})}^{(\mathrm{ins})\prime}$ above 0.2 Hz for both models.

The recordings by almost all stations [for which $\delta t_i^{(\mathrm{ins})}$ needed to be estimated) appear to be subject to a time delay, i.e. a negative $\tilde{\delta t}_{i(\mathrm{wls})}^{(\mathrm{ins})\prime}$]. This in line with both our observations in Fig. 2 (and Figs S4 and S5) and the computed *a priori* estimates (presented in Fig. S7). In particular for the OBSs, this is not surprising as these usually incur time delays over time (e.g. Takeo *et al*. 2014; Hable *et al*. 2018). Of course, the recovered timing errors are an average timing error for the entire recording period, since they are based on time-averaged cross-correlations. By computing time-lapse ambient noise cross-correlations, however, a procedure similar to the one presented in this work could be used to estimate the actual (linear) clock drift. This involves making $\delta t_i^{(\mathrm{ins})}$ linearly dependent on the time $t^{(\mathrm{lps})}$ at which these time-lapse cross-correlations centre, that is, $\delta t_i^{(\mathrm{ins})}(t^{(\mathrm{lps})}) = a_i t^{(\mathrm{lps})} + b_i$. Substitution in eq. (5) subsequently yields a time-dependent $\left(t_{i,j}^{(+,\mathrm{app})} + t_{i,j}^{(-,\mathrm{app})}\right)(t^{(\mathrm{lps})})$. In case one possesses time-lapse cross-correlations associated with two or more different $t^{(\mathrm{lps})}$, a matrix formulation similar to eq. (6) may then be obtained. This set of equations would, in principle, allow one to invert for the a_i and b_i, which are of course station-specific (hence allowing different stations to have different drift rates). We are currently further investigating this.

10 CONCLUSIONS

We have derived a formulation that allows instrumental timing errors to be recovered using time-averaged receiver–receiver cross-correlations. The formulation exploits the theoretical time-symmetry of these cross-correlations, which holds for time-averaged cross-correlations of ambient seismic noise propagating with equal intensity in all directions. In particular, we consider time-averaged cross-correlations of ambient seismic surface-wave noise. We show that by quantifying the difference between the arrival time of the direct surface-wave at positive time and the arrival time of the direct surface-wave at negative time for a large a number of receiver–receiver pairs, the unknown instrumental timing errors can be recovered using an ordinary least-squares inversion, provided the timing of at least one of the receivers is known to be correct. In the absence of a uniform surface-wave illumination, however, the time-symmetry of the time-averaged receiver–receiver cross-correlations is broken. Consequently, instrumental timing errors recovered using the ordinary least-squares inversion will be subject to errors. We show that in this case a weighted least-squares inversion, where receiver pairs are weighted by their receiver–receiver separation, reduces these errors. Considering the station configuration of the RARR, we validated the method using synthetic surface-wave (noise) recordings. We subsequently applied the weighted inversion to field recordings of ambient seismic noise on and around the Reykjanes peninsula, SW Iceland. We find the recordings by all ocean bottom seismometers to be subject to time delays between 0 and 1 s.

ACKNOWLEDGEMENTS

We are grateful to the institute of geophysics of the CAS for using the data recorded by the REYKJANET stations. Specifically, we would like to thank Jakub Klicpera, Bohuslav Ruzek and Josef Horalek. Similarly, we thank the Icelandic meteorological office (MET office) and Iceland GeoSurvey (ISOR) for allowing us to use their data (ISOR and SIL networks, respectively). Instruments for the IMAGE project were provided by the GIPP (Geophysical Instrument pool Potsdam) and the DEPAS (German instrument pool for amphibian seismology).

Lucia Gualtieri we warmly thank for providing us with the surface-wave dispersion data used to model ambient noise surface-waves. This study benefited from interactions with Pavel Ditmar, Shohei Minato, Jan Thorbecke, Philippe Jousset, Hanna Blanck, Hanneke Paulssen, Kristján Ágústsson and Gylfi Páll Hersir. The research leading to these results has received funding from the European Community's Seventh Framework Programme under grant agreement No. 608553 (Project IMAGE). The contribution of PS is funded through a VIDI project from the Netherlands Organisation for Scientific Research (NWO), Project 864.14.005. During part of this project, CW was supported by the Netherlands Research Centre for Integrated Solid Earth Sciences (ISES). Figures were generated with the help of Generic Mapping Tools (e.g. Wessel *et al*. 2019). We thank Akiko Takeo and one anonymous reviewer for their detailed and constructive reviews. The data used this study are not immediately openly available, but please contact the authors and we may well be able to accomodate your request. The FORTRAN code used to estimate the (station couple specific) arrival-time differences and solve the inverse problems is available at https://github.com/kweemstra/recover_timing_errors.

REFERENCES

Aki, K. & Richards, P.G., 2002. *Quantitative Seismology,* 2nd edn. University Science Books.

Bakulin, A. & Calvert, R., 2006. The virtual source method: theory and case study, *Geophysics,* **71**(4), SI139–SI150.

Boas, M.L., 2006. *Mathematical Methods in the Physical Sciences,* 3rd edn. John Wiley \& Sons.

Boschi, L. & Weemstra, C., 2015. Stationary-phase integrals in the cross-correlation of ambient noise, *Rev. Geophys.,* **53,** 411–451.

Bromirski, P.D., Duennebier, F.K. & Stephen, R.A., 2005. Mid-ocean microseisms, *Geochem. Geophys. Geosyst.,* **6**(4), doi:10.1029/2004GC000768.

Cox, C., Deaton, T. & Webb, S., 1984. A deep-sea differential pressure gauge, *J. Atmos. Ocean. Technol.,* **1**(3), 237–246.

Dziewonski, A.M. & Anderson, D.L., 1981. Preliminary reference Earth model, *Phys. Earth planet. Inter.,* **25**(4), 297–356.

Ekström, G., Abers, G. & Webb, S., 2009. Determination of surface-wave phase velocities across USArray from noise and Aki's spectral formulation, *Geophys. Res. Lett.,* **36**(18), L18301.

Froment, B., Campillo, M., Roux, P., Gouédard, P., Verdel, A. & Weaver, R.L., 2010. Estimation of the effect of nonisotropically distributed energy on the apparent arrival time in correlations, *Geophysics,* **75**(5), SA85–SA93.

Gerstoft, P., Shearer, P.M., Harmon, N. & Zhang, J., 2008. Global P, PP, and PKP wave microseisms observed from distant storms, *Geophys. Res. Lett.,* **35**(23), L23306.

Gouédard, P., Seher, T., McGuire, J.J., Collins, J.A. & van der Hilst, R.D., 2014. Correction of ocean-bottom seismometer instrumental clock errors using ambient seismic noise, *Bull. seism. Soc. Am.,* **104**(3), 1276–1288.

Gualtieri, L., Stutzmann, E., Capdeville, Y., Ardhuin, F., Schimmel, M., Mangeney, A. & Morelli, A., 2013. Modelling secondary microseismic noise by normal mode summation, *Geophys. J. Int.,* **193**(3) 1732–1745.

Hable, S., Sigloch, K., Barruol, G., Stähler, S.C. & Hadziioannou, C., 2018. Clock errors in land and ocean bottom seismograms: high-accuracy estimates from multiple-component noise cross-correlations, *Geophys. J. Int.,* **214**(3), 2014–2034.

Halliday, D. & Curtis, A., 2008. Seismic interferometry, surface-waves and source distribution, *Geophys. J. Int.,* **175**(3), 1067–1087.

Hanasoge, S.M., 2013. The influence of noise sources on cross-correlation amplitudes, *Geophys. J. Int.,* **192**(1), 295–309.

Hanasoge, S.M. & Branicki, M., 2013. Interpreting cross-correlations of one-bit filtered seismic noise, *Geophys. J. Int.,* **193,** 1811–1830.

Hannemann, K., Krüger, F. & Dahm, T., 2013. Measuring of clock drift rates and static time offsets of ocean bottom stations by means of ambient noise, *Geophys. J. Int.,* **196**(2), 1034–1042.

Harmon, N., Rychert, C. & Gerstoft, P., 2010. Distribution of noise sources for seismic interferometry, *Geophys. J. Int.,* **183**(3), 1470–1484.

Hasselmann, K., 1963. A statistical analysis of the generation of microseisms, *Rev. Geophys.,* **1**(2), 177–210.

Hatchell, P. & Mehta, K., 2010. Ocean-bottom seismic (OBS) timing drift correction using passive seismic data, *SEG Tech. Prog. Expand. Abstr.,* **29,** 2054–2058.

Jin, G. & Gaherty, J.B., 2015. Surface-wave phase-velocity tomography based on multichannel cross-correlation, *Geophys. J. Int.,* **201**(3), 1383–1398.

Kästle, E.D., Soomro, R., Weemstra, C., Boschi, L. & Meier, T., 2016. Two-receiver measurements of phase velocity: cross-validation of ambient-noise and earthquake-based observations, *Geophys. J. Int.,* **207,** 1493–1512.

Kimman, W.P., Campman, X. & Trampert, J., 2012. Characteristics of seismic Noise: fundamental and higher mode energy observed in the northeast of the Netherlands, *Bull. seism. Soc. Am.,* **102**(4), 1388–1399.

Lacoss, R.T., Kelly, E.J. & Toksoz, M.N., 1969. Estimation of seismic noise structure using arrays, *Geophysics,* **34,** 21–38.

Le, B.M., Yang, T., Chen, Y.J. & Yao, H., 2018. Correction of OBS clock errors using Scholte waves retrieved from cross-correlating hydrophone recordings, *Geophys. J. Int.,* **212,** 891–899.

Lin, F.C., Tsai, V.C. & Ritzwoller, M.H., 2012. The local amplification of surface-waves: a new observable to constrain elastic velocities, density, and anelastic attenuation, *J. geophys. Res.: Solid Earth,* **117**(B06), B06302.

Lindner, F., Weemstra, C., Walter, F. & Hadziioannou, C., 2018. Towards monitoring the Englacial fracture state using virtual-reflector seismology, *Geophys. J. Int.,* **214**(2), 825–844.

Longuet-Higgins, M.S., 1950. A theory of the origin of microseisms, *Phil. Trans. R. Soc. Lond., A,* **243**(857), 1–35.

Malcolm, A.E., Scales, J.A. & Van Tiggelen, B.A., 2004. Extracting the Green function from diffuse, equipartitioned waves, *Phys. Rev. E,* **70**(1 2), 1–4.

Martins, J.E., Weemstra, C., Ruigrok, E., Verdel, A., Jousset, P. & Hersir, G.P., 2020. 3D S-wave velocity imaging of Reykjanes Peninsula high-enthalpy geothermal fields with ambient-noise tomography, *J. Volc. Geother. Res.,* **391,** 106685.

Melton, B.S. & Bailey, L.F., 1957. Multiple signal correlators, *Geophysics,* **XXII**(3), 565–588.

Mulargia, F., 2012. The seismic noise wavefield is not diffuse, *J. acoust. Soc. Am.,* **131**(4), 2853.

Obermann, A., Froment, B., Campillo, M., Larose, E., Planès, T., Valette, B., Chen, J.H. & Liu, Q.Y., 2014. Seismic noise correlations to image structural and mechanical changes associated with the Mw 7.9 2008 Wenchuan earthquake, *J. geophys. Res.,* **119,** 3155–3168.

Olson, J.V., 2004. Infrasound signal detection using the Fisher F-Statistic, *Inframatics,* **6,** 1–7.

Poli, P., Pedersen, H.A. & Campillo, M., the POLENET/LAPNET Working Group, 2012. Emergence of body waves from cross-correlation of short period seismic noise, *Geophys. J. Int.,* **188**(2), 549–558.

Rao, C.R., 1973. *Linear Statistical Inference and its Applications,* 2nd edn. John Wiley \& Sons.

Rost, S. & Thomas, C., 2002. Array seismology: methods and applications, *Rev. Geophys.,* **40**(3), 2–1-2-27.

Seats, K.J., Lawrence, J.F. & Prieto, G.A., 2012. Improved ambient noise correlation functions using Welch's method, *Geophys. J. Int.,* **188**(2), 513–523.

Sens-Schönfelder, C., 2008. Synchronizing seismic networks with ambient noise, *Geophys. J. Int.,* **174**(3), 966–970.

Shapiro, N.M. & Campillo, M., 2004. Emergence of broadband Rayleigh waves from correlations of the ambient seismic noise, *Geophys. Res. Lett.,* **31**(7), L07614.

Shariat-Panahi, S., Alegria, F.C., Làzaro, A.M. & del Rio, J., 2009. Time drift of ocean bottom seismometers (OBS), in *Proceedings of the 19th IMEKO World Congress on Fundamental and Applied Metrology,* pp. 2548–2553.

Shimizu, S., Katagiri, M., Watarai, Y., Ueda, Y., Sack, P. & Gonzalez, F., 2019. Semipermanent ocean-bottom seismic node: toward practical reservoir monitoring, *Leading Edge,* **38**(9), 716–719.

Snieder, R., 2004. Extracting the Green's function from the correlation of coda waves: a derivation based on stationary phase, *Phys. Rev. E,* **69**(4), 46610.

Snieder, R. & Trampert, J., 1999. Inverse problems in geophysics, in *Wavefield Inversion,* pp. 119–190ed. Wirgin, A., Springer-Verlag.

Stehly, L., Campillo, M. & Shapiro, N.M., 2006. A study of the seismic noise from its long-range correlation properties, *J. geophys. Res.,* **111**(B10), B10306, doi:10.1029/2005JB004237.

Stehly, L., Campillo, M. & Shapiro, N.M., 2007. Traveltime measurements from noise correlation: stability and detection of instrumental time shifts, *Geophys. J. Int.,* **171**(1), 223–230.

Takeo, A., Forsyth, D.W., Weeraratne, D.S. & Nishida, K., 2014. Estimation of azimuthal anisotropy in the NW Pacific from seismic ambient noise in seafloor records, *Geophys. J. Int.,* **199**(1), 11–22.

Tsai, V.C., 2009. On establishing the accuracy of noise tomography traveltime measurements in a realistic medium, *Geophys. J. Int.,* **178**(3), 1555–1564.

Tsai, V.C., 2010. The relationship between noise correlation and the Green's function in the presence of degeneracy and the absence of equipartition, *Geophys. J. Int.,* **182**(3), 1509–1514.

Tsai, V.C., 2011. Understanding the amplitudes of noise correlation measurements, *J. geophys. Res.,* **116**(B09), B09311, doi:10.1029/2011JB008483.

van Wijk, K., Mikesell, T.D., Schulte-Pelkum, V. & Stachnik, J., 2011. Estimating the Rayleigh-wave impulse response between seismic stations with the cross terms of the Green tensor, *Geophys. Res. Lett.,* **38**(16), L16301.

Virieux, J. & Operto, S., 2009. An overview of full-waveform inversion in exploration geophysics, *Geophysics,* **74**(6), WCC127–WCC152.

Wapenaar, K. & Fokkema, J., 2006. Green's function representations for seismic interferometry, *Geophysics,* **71**(4), SI33–SI46.

Warner, M. & Guasch, L., 2014. Adaptive waveform inversion - FWI without cycle skipping - theory, in *Proceedings of the 76th Conference and Exhibition, EAGE, Expanded Abstracts*.

Weaver, R., Froment, B. & Campillo, M., 2009. On the correlation of non-isotropically distributed ballistic scalar diffuse waves., *J. acoust. Soc. Am.,* **126**(4), 1817–1826.

Weemstra, C., Boschi, L., Goertz, A. & Artman, B., 2013. Seismic attenuation from recordings of ambient noise, *Geophysics,* **78**(1), Q1–Q14.

Weemstra, C., Westra, W., Snieder, R. & Boschi, L., 2014. On estimating attenuation from the amplitude of the spectrally whitened ambient seismic field, *Geophys. J. Int.,* **197,** 1770–1788.

Weemstra, C., Draganov, D., Ruigrok, E.N., Hunziker, J., Gomez, M. & Wapenaar, K., 2017. Application of seismic interferometry by multidimensional deconvolution to ambient seismic noise recorded in Malargüe, Argentina, *Geophys. J. Int.,* **208**(2), 693–714.

Wessel, P., Luis, J.F., Uieda, L., Scharroo, R., Wobbe, F., Smith, W.H. & Tian, D., 2019. The generic mapping tools version 6, *Geochem. Geophys. Geosyst.,* **20**(11), 5556–5564.

Yang, Y. & Ritzwoller, M.H., 2008. Characteristics of ambient seismic noise as a source for surface-wave tomography, *Geochem. Geophys. Geosyst.,* **9**(2), Q02008.

Ye, F., Lin, J., Shi, Z. & Lyu, S., 2018. Monitoring temporal variations in instrument responses in regional broadband seismic network using ambient seismic noise, *Geophys. Prospect.,* **66**(5), 1019–1036.

SUPPORTING INFORMATION

Supplementary data are available at *GJI* online.

Figure S1 Data availability for each of the stations of the RARR during 2014 and 2015. Stations O[01-26] are ocean bottom seismometers. The stations' network codes and instrument types can be found in table 1 of the paper.

Figure S2 Theoretical phase response for the various instrument types constituting the RARR.

Figure S3 Theoretical amplitude response (normalized with respect to amplitude at 1 Hz) for the various instrument types constituting the RARR.

Figure S4 Analysis of the surface-waves generated by a M_w 5.5 earthquake along the Mid-Atlantic Ridge at a distance of approximately 940 km. (a) The surface-waves, filtered between 0.1 and 0.2 Hz, recorded by station SKH$^{\checkmark}$ (note that body wave energy is negligible in this frequency band). (b) Zoom of the earthquake's surface-waves recorded by the IMAGE stations STF$^{\checkmark}$, LFE$^{\checkmark}$ and SKH$^{\checkmark}$. A trace's position along the vertical axis increases proportional to its increase in distance from the earthquake's epicentre. (c) Same as (b), but including two REYKJANET stations. (d) Locations of the stations (depicted area is approximately 15 by 10 km). The arrow indicates the approximate direction of propagation of the surface-wave train indicated in green in a, as determined by frequency–wavenumber analysis at 0.16 Hz using the only the three IMAGE stations. (e) Result of frequency–wavenumber analysis at 0.16 Hz using only the three IMAGE stations. Beamformer output is given as function of horizontal and vertical slowness (p_x and p_y, respectively). (f) Unwrapped phase at 0.16 Hz. Phases are obtained through Fourier transformation of the surface-waves arriving in the time window for which frequency–wavenumber analysis was performed. The slope of the solid black line corresponds to the slowness indicated by the yellow star in (e) (i.e. the so-called 'best beam'). This line is subsequently fitted, in least-squares sense, to the unwrapped phases of the three IMAGE stations.

Figure S5 Analysis of the surface-waves generated by a M_w 5.5 earthquake in Iceland at a distance of approximately 260 km from the tip of the Reykjanes peninsula. (a) The surface-waves, filtered between 0.1 and 0.2 Hz, recorded by station RAR$^{\checkmark}$ (note that body wave energy is negligible in this frequency band). (b) Zoom of the earthquake's surface-waves recorded by nine IMAGE stations. A trace's position along the vertical axis increases proportional to its increase in distance from the earthquake's epicentre. (c) Same as (b), but including the 8 ISOR stations and one SIL station (RNE$^{\times}$) . (d) Location of the stations located on the tip of the peninsula. The arrow indicates the approximate direction of propagation of the surface-wave train indicated in green in a, as determined by frequency–wavenumber analysis at 0.133 Hz using only the nine IMAGE stations. (e) Result of frequency–wavenumber analysis at 0.133 Hz using only the nine IMAGE stations. Beamformer output is given as function of horizontal and vertical slowness (p_x and p_y, respectively). (f) Unwrapped phase at 0.133 Hz. Phases are obtained through Fourier transformation of the surface-waves arriving in the time window for which frequency–wavenumber analysis was performed. The slope of the solid black line corresponds to the slowness indicated by the yellow star in e (i.e. the so-called 'best beam'). This line is subsequently fitted, in least-squares sense, to the unwrapped phases of the nine IMAGE stations.

Figure S6 Comparison of the application of SI to the station couples HAH✓–SKG✓ and HAH✓–ISS✗. Stations HAH✓ and SKG✓ are separated by 16.85 km, and stations HAH✓ and ISS✗ are separated by 18.04 km. (a) Station locations and ray paths. (b) The time averaged cross-correlation is shown for three different frequency bands (time averaged cross-correlation of the recordings by HAH✓ and SKG✓ is depicted as a black solid line; time averaged cross-correlation of the recordings by HAH✓ and ISS✗ is depicted as a lightblue solid line). (c) The real part of the cross-spectrum (dots) with the linear combination of third-order polynomials that best fits their behaviour overlain (solid lines) for both station couples. (d) Velocity values (triangles) for which the zeros of a zeroth order Bessel function of the first kind coincide with the zeros of the least-squares fits in (c) [the procedure is similar to the approach by Ekström *et al*. (2009) and explained in detail in Lindner *et al*. (2018)]. Rayleigh wave fundamental-mode phase velocities for the preliminary reference earth model (PREM, but with the oceanic layer removed; Dziewonski & Anderson 1981) are given by the grey dashed curve. The PREM dispersion curve is used to determine the seismologically most plausible dispersion curves (black solid curve for station couple HAH✓–SKG✓; lightblue solid curve for station couple HAH✓–ISS✗). For details regarding the picking of these phase velocity curves we refer to Kästle *et al*. (2016).

Figure S7 The $\delta t^{(\mathrm{ins,\,ap})}$ for all ISOR and SIL stations. The estimation of $\delta t^{(\mathrm{ins,\,ap})}$ at 0.09 Hz using the event close to Chile (orange dots) is visualized in Fig. 6 of the paper. We did not determine $\delta t^{(\mathrm{ins,\,ap})}$ for the OBSs, because, for most of them, there are no nearby stations for which the timing is guaranteed. In addition, the potential timing errors of the OBSs attributed to clock drift are expected to be in the order of a few seconds only (e.g. Hannemann *et al*. 2013)

Figure S8 (a) Difference between the $t_{i,j}^{(+,\mathrm{app})} + t_{i,j}^{(-,\mathrm{app})}$ (i.e. the measurements) and $2\tilde{\delta t}_{i(\mathrm{wls})}^{(\mathrm{ins})\prime} - 2\tilde{\delta t}_{j(\mathrm{wls})}^{(\mathrm{ins})\prime}$ at $f_c = 0.20$ Hz. The latter are recovered using the the weighted-least squares inversion that takes into account deviations of the mean of the noise from zero. These values are recovered using time-averaged cross-correlations with a SNR higher than 25, and for which the stations are separated by more than 3 wavelengths (computed based on the reference phase-velocity dispersion curves). (b) Histogram with the mean of the values in (a) for each station. The fact that these values are lower than 0.1 s for all station couples is a direct consequence of the relatively accurate recovery of the $\delta t_i^{(\mathrm{ins})}$, compared to the recovery using time-averaged cross-correlations with a SNR that is also higher than 25, but for which the stations are separated by more than 3.25 wavelengths (see Fig. S9). This higher accuracy is manifested by the large 'drop' in the mean absolute residual error in Fig. 10 of the paper (sudden transition from red to blue). (c) Histogram indicating the number of eligible station couples for each station, for this specific SNR threshold and $r^{(\lambda\text{-trh})} = 3.0$.

Figure S9 (a) Difference between the $t_{i,j}^{(+,\mathrm{app})} + t_{i,j}^{(-,\mathrm{app})}$ (i.e. the measurements) and $2\tilde{\delta t}_{i(\mathrm{wls})}^{(\mathrm{ins})\prime} - 2\tilde{\delta t}_{j(\mathrm{wls})}^{(\mathrm{ins})\prime}$ at $f_c = 0.20$ Hz. The latter are recovered using the the weighted-least squares inversion that takes into account deviations of the mean of the noise from zero. These values are recovered using time-averaged cross-correlations with a SNR higher than 25, and for which the stations are separated by more than 3.25 wavelengths (computed based on the reference phase-velocity dispersion curves). (b) Histogram with the mean of the values in a for each station. Station couples involving two specific stations exhibit particularly large differences, which is a direct consequence of the inaccurate recovery of the $\delta t_i^{(\mathrm{ins})}$ of these two stations. In particular, if compared to the results of the inversion using time-averaged cross-correlations with a SNR that is also higher than 25, but for which the stations are separated by more than 3.00 wavelengths (see Fig. S8). The lower accuracy is manifested by the large 'jump' in the mean absolute residual error in Fig. 10 of the paper (sudden transition from blue to red). (c) Histogram indicating the number of eligible station couples for each station, for this specific SNR threshold and $r^{(\lambda\text{-trh})} = 3.25$.

Please note: Oxford University Press is not responsible for the content or functionality of any supporting materials supplied by the authors. Any queries (other than missing material) should be directed to the corresponding author for the paper.

APPENDIX A: THE MATRIX A AND THE VECTORS $\mathbf{t}^{(\mathrm{ins})}$, $\mathbf{n}^{(\mathrm{src})}$, $\mathbf{n}^{(\mathrm{spur})}$ AND $\mathbf{t}^{(\mathrm{app})}$

In case we possess synchronous noise recordings by a total of N seismic stations, a maximum of $N(N-1)/2$ time-averaged cross-correlations can be obtained. Assuming that $t_{i,j}^{(+,\mathrm{app})}$ and $t_{i,j}^{(-,\mathrm{app})}$ can be determined for all time-averaged cross-correlations, the following system of equations is obtained,

$$\mathbf{A}\mathbf{t}^{(\mathrm{ins})} + \mathbf{n}^{(\mathrm{src})} + \mathbf{n}^{(\mathrm{spur})} = \mathbf{t}^{(\mathrm{app})}, \tag{6}$$

|08-865e the matrices $\mathbf{A}$, $\mathbf{t}^{(\mathrm{ins})}$, $\mathbf{n}^{(\mathrm{src})}$, $\mathbf{n}^{(\mathrm{spur})}$ and $\mathbf{t}^{(\mathrm{app})}$, have the following form:

$$\mathbf{A} \equiv \overset{7}{\begin{pmatrix} 2 & -2 & 0 & \cdots & \cdots & 0 \\ 2 & 0 & -2 & 0 & \cdots & 0 \\ \vdots & \vdots & \ddots & \ddots & \ddots & \vdots \\ 2 & 0 & 0 & \cdots & 0 & -2 \\ 0 & 2 & -2 & \cdots & \cdots & 0 \\ 0 & 2 & 0 & -2 & \cdots & 0 \\ \vdots & \vdots & \vdots & \ddots & \ddots & \vdots \\ 0 & 2 & 0 & \cdots & 0 & -2 \\ \vdots & \vdots & \vdots & \vdots & \vdots & \vdots \\ 0 & \cdots & 0 & 2 & -2 & 0 \\ 0 & \cdots & 0 & 2 & 0 & -2 \\ 0 & \cdots & \cdots & 0 & 2 & -2 \end{pmatrix}}, \tag{A.1}$$

$$\mathbf{t}^{(\mathrm{ins})} \equiv \begin{pmatrix} \delta t_1^{(\mathrm{ins})} \\ \delta t_2^{(\mathrm{ins})} \\ \vdots \\ \delta t_N^{(\mathrm{ins})} \end{pmatrix}, \tag{A.2}$$

$$\mathbf{n}^{(\mathrm{src})} \equiv \begin{pmatrix} \delta t_{1,2}^{(+,\mathrm{src})} + \delta t_{1,2}^{(-,\mathrm{src})} \\ \delta t_{1,3}^{(+,\mathrm{src})} + \delta t_{1,3}^{(-,\mathrm{src})} \\ \vdots \\ \delta t_{1,N}^{(+,\mathrm{src})} + \delta t_{1,N}^{(-,\mathrm{src})} \\ \delta t_{2,3}^{(+,\mathrm{src})} + \delta t_{2,3}^{(-,\mathrm{src})} \\ \delta t_{2,4}^{(+,\mathrm{src})} + \delta t_{2,4}^{(-,\mathrm{src})} \\ \vdots \\ \delta t_{2,N}^{(+,\mathrm{src})} + \delta t_{2,N}^{(-,\mathrm{src})} \\ \vdots \\ \delta t_{N-2,N-1}^{(+,\mathrm{src})} + \delta t_{N-2,N-1}^{(-,\mathrm{src})} \\ \delta t_{N-2,N}^{(+,\mathrm{src})} + \delta t_{N-2,N}^{(-,\mathrm{src})} \\ \delta t_{N-1,N}^{(+,\mathrm{src})} + \delta t_{N-1,N}^{(-,\mathrm{src})} \end{pmatrix}, \tag{A.3}$$

$$\mathbf{n}^{(\mathrm{spur})} \equiv \begin{pmatrix} \delta t_{1,2}^{(+,\mathrm{spur})} + \delta t_{1,2}^{(-,\mathrm{spur})} \\ \delta t_{1,3}^{(+,\mathrm{spur})} + \delta t_{1,3}^{(-,\mathrm{spur})} \\ \vdots \\ \delta t_{1,N}^{(+,\mathrm{spur})} + \delta t_{1,N}^{(-,\mathrm{spur})} \\ \delta t_{2,3}^{(+,\mathrm{spur})} + \delta t_{2,3}^{(-,\mathrm{spur})} \\ \delta t_{2,4}^{(+,\mathrm{spur})} + \delta t_{2,4}^{(-,\mathrm{spur})} \\ \vdots \\ \delta t_{2,N}^{(+,\mathrm{spur})} + \delta t_{2,N}^{(-,\mathrm{spur})} \\ \vdots \\ \delta t_{N-2,N-1}^{(+,\mathrm{spur})} + \delta t_{N-2,N-1}^{(-,\mathrm{spur})} \\ \delta t_{N-2,N}^{(+,\mathrm{spur})} + \delta t_{N-2,N}^{(-,\mathrm{spur})} \\ \delta t_{N-1,N}^{(+,\mathrm{spur})} + \delta t_{N-1,N}^{(-,\mathrm{spur})} \end{pmatrix}, \tag{A.4}$$

and

$$\mathbf{t}^{(\mathrm{app})} \equiv \begin{pmatrix} t_{1,2}^{(+,\mathrm{app})} + t_{1,2}^{(-,\mathrm{app})} \\ t_{1,3}^{(+,\mathrm{app})} + t_{1,3}^{(-,\mathrm{app})} \\ \vdots \\ t_{1,N}^{(+,\mathrm{app})} + t_{1,N}^{(-,\mathrm{app})} \\ t_{2,3}^{(+,\mathrm{app})} + t_{2,3}^{(-,\mathrm{app})} \\ t_{2,4}^{(+,\mathrm{app})} + t_{2,4}^{(-,\mathrm{app})} \\ \vdots \\ t_{2,N}^{(+,\mathrm{app})} + t_{2,N}^{(-,\mathrm{app})} \\ \vdots \\ t_{N-2,N-1}^{(+,\mathrm{app})} + t_{N-2,N-1}^{(-,\mathrm{app})} \\ t_{N-2,N}^{(+,\mathrm{app})} + t_{N-2,N}^{(-,\mathrm{app})} \\ t_{N-1,N}^{(+,\mathrm{app})} + t_{N-1,N}^{(-,\mathrm{app})} \end{pmatrix}. \tag{A.5}$$

The rows and columns of $\mathbf{A}$ relate to different station pairs and stations, respectively. Each row has only two non-zero elements, of which the element associated with the lowest column index is 2, and the element associated with the highest column index –2. The column vector $\mathbf{t}^{(\mathrm{ins})}$ holds the N instrumental timing errors, and the column vectors $\mathbf{n}^{(\mathrm{src})}$, $\mathbf{n}^{(\mathrm{spur})}$ and $\mathbf{t}^{(\mathrm{app})}$ hold the $N(N-1)/2$ combinations of $\delta t_{i,j}^{(+,\mathrm{src})} + \delta t_{i,j}^{(-,\mathrm{src})}$, $\delta t_{i,j}^{(+,\mathrm{spur})} + \delta t_{i,j}^{(-,\mathrm{spur})}$ and $t_{i,j}^{(+,\mathrm{app})} + t_{i,j}^{(-,\mathrm{app})}$, respectively. Perhaps not surprisingly, the matrix $\mathbf{A}$ in eq. (A.1) spans a space of $N-1$ dimensions. This can be verified by Gaussian elimination of $\mathbf{A}$ (e.g. Boas 2006): subtracting from each row of $\mathbf{A}$ with nonadjacent non-zero elements k and l that row of $\mathbf{A}$ with non-zero elements $k+1$ and l, one is left with $N-1$ unique rows.

As explained in the main text, it is in practice often not feasible to estimate both $t_{i,j}^{(+,\mathrm{app})}$ and $t_{i,j}^{(-,\mathrm{app})}$ from all $C_{i,j}$. As long as each station is indirectly 'linked' to all other stations, however, the rank of $\mathbf{A}$ remains $N-1$. For example, in the extreme case that the arrival times at positive and negative time can only be determined from the $N-1$ time-averaged cross-correlations $C_{1,2}$, $C_{2,3}$, $C_{3,4}$, ..., $C_{N-1,N}$, the matrix $\mathbf{A}$ has still rank $N-1$. A consequence of this so-called rank deficiency is that a unique solution vector $\mathbf{t}^{(\mathrm{ins})}$ can only be obtained if one knows at least one $\delta t_i^{(\mathrm{ins})}$. In other words, one always has to be certain about the timing of at least one station.

APPENDIX B: THE VECTORS ASSOCIATED WITH THE WEIGHTED LEAST-SQUARES SOLUTION

In the body of the paper, we introduced

$$\mathbf{n}^{(\mathrm{src})} = \mathbf{f} \odot \mathbf{n}^{(\mathrm{azi})}, \tag{19}$$

where $\odot$ denotes Hadamard matrix multiplication (i.e. element-wise multiplication). In case we possess synchronous noise recordings by a total of N seismic stations, and assuming that $t_{i,j}^{(+,\mathrm{app})}$ and $t_{i,j}^{(-,\mathrm{app})}$ can be determined for all time-averaged cross-correlations, $\mathbf{f}$ and $\mathbf{n}^{(\mathrm{azi})}$ have the following form:

$$\mathbf{f} \equiv \begin{pmatrix} 1/t_{1,2} \\ 1/t_{1,3} \\ \vdots \\ 1/t_{1,N} \\ 1/t_{2,3} \\ 1/t_{2,4} \\ \vdots \\ 1/t_{2,N} \\ \vdots \\ 1/t_{N-2,N-1} \\ 1/t_{N-2,N} \\ 1/t_{N-1,N} \end{pmatrix} \tag{B.1}$$

and

$$\mathbf{n}^{(\mathrm{azi})} \equiv \begin{pmatrix} \delta t_{1,2}^{(\mathrm{azi})} \\ \delta t_{1,3}^{(\mathrm{azi})} \\ \vdots \\ \delta t_{1,N}^{(\mathrm{azi})} \\ \delta t_{2,3}^{(\mathrm{azi})} \\ \delta t_{2,4}^{(\mathrm{azi})} \\ \vdots \\ \delta t_{2,N}^{(\mathrm{azi})} \\ \vdots \\ \delta t_{N-2,N-1}^{(\mathrm{azi})} \\ \delta t_{N-2,N}^{(\mathrm{azi})} \\ \delta t_{N-1,N}^{(\mathrm{azi})} \end{pmatrix}. \tag{B.2}$$